Verschueren van Rees, N., & Champneys, A. R. (2017). A Model for Cell Polarization Without Mass Conservation. *SIAM Journal on Applied Dynamical Systems*, *16*(4), 1797-1830. https://doi.org/10.1137/16M1093847

A model for cell polarisation without mass conservation.

Nicolas Verschueren* and Alan Champneys†

Abstract. A system of two Schnakenberg-like reaction-diffusion equations is investigated analytically and numerically. The system has previously been used as a minimal model for concentrations of GTPases involved in the process of cell polarisation. Source and loss terms are added, breaking the mass conservation, which was shown previously to be responsible for the generation of stable fronts via a so-called wave-pinning mechanism. The extended model gives rise to a unique homogeneous equilibrium in the parameter region of interest, which loses stability via a pattern formation, or Turing bifurcation. The bistable character of the reaction terms ensures that this bifurcation is subcrtical for sufficiently small values of the driving parameter multiplying the nonlinear kinetics. This subcriticality leads to the onset of a multitude of localised solutions, through the homoclinic snaking mechanism. As the driving parameter is further decreased, the multitude of solutions transforms into a single pulse through a Belyakov-Devaney transition in which there is the loss of a precursive pattern. An asymptotic analysis is used to probe the conservative limit in which the source and loss terms vanish. Matched asymptotic analysis shows that on an infinite domain the pulse solution transitions into a pair of fronts, with an additional weak quadratic core and exponential tails. On a finite domain, the core and tails disappear, leading to the mere wave-pinning front and its mirror image.

Key words. Reaction-diffusion systems, Cell polarisation, G-proteins.

AMS subject classifications. 35B25, 35B32, 35K57, 34B07.

1. Introduction.

Eukaryotic cell polarisation is the process by which a cell forms two distinct spatial domains a "front-end" and a "back-end", defining a polarisation axis. This process is the first step in many vital cellular processes such as cell differentiation, wound healing, cell motility and organelle organisation. Roughly speaking, cell polarisation can be described as the symmetry-breaking presented by the spatial concentration of certain proteins and lipids inside the cell [17]. Polarisation may be caused spontaneously or by some external trigger or stimulus, here we shall consider the polarisation induced by an external stimulus, acting on the spatially heterogeneous concentration of certain GTPases, also known as G-proteins or Rho's. See section 2 below for background information.

The spatio-temporal dynamics of Rho-GTPases within a single cell has been described using reaction-diffusion models; see [12, 17, 35]. Minimal models consider just one GTPase, present in both active and inactive forms. Examples of such models were proposed by Meinhardt [24] and, with the explicit introduction of mass conservation, by Otsuji *et al.* [29]. These works presume that the fundamental mechanism for spatial symmetry breaking is the so-called diffusion driven or Turing instability, see e.g. [28]. This mechanism is appealing, because there is a natural discrepancy between the diffusion rates of the free, inactive GTPases and their membrane-bound active counterparts. However, the Turing mechanism is known to lead to

*Department of Engineering Mathematics, University of Bristol, Queen's Building, University Walk, Bristol BS8 1TR, United Kingdom (n.verschuerenvanrees@bristol.ac.uk)

†Department of Engineering Mathematics, University of Bristol, Merchant Venturers Building, Woodland Road, Clifton BS8 1UB (A.R.Champneys@bristol.ac.uk)

patterns characterised by a specific spatial wavelength rather than a single front or pulse — see. Figure 1(a,b) below. (Note though that the assumption in these works is that of supercritical Turing bifurcations; it is argued in [3] that subcritical Turing bifurcations naturally lead to spatially localised states through the so-called homoclinic snaking mechanism [1, 39]). Additionally, the timescale required for the break of symmetry in the Turing instability was found not to match those observed experimentally; see [17] for details.

In order to overcome these difficulties, Mori *et al.* [26], proposed a rather different mechanism, called *wave pinning*, in which a single front is set up between two different asymptotic levels of the active G-protein. The pinning mechanism is different from that of scalar reaction-diffusion equations and relies on the resting position of a moving front being set by the overall mass conservation of active and inactive species (see section 3 below for a concise argument). Once the front is established, the polarity can be inverted (the spatial reflection of the original front) through new stimuli, a feature which is observed in the experiments. This minimal model has also served as the basis for more complex models in cell motility (see [23] and references therein).

The minimal models describing the dynamics of a single GTPase are intended to be prototype models. However they have been successfully fit to experimental data [22]. The simplicity of these models allows analytic calculations which enable us to uncover the essential mechanism responsible for cell polarisation. In [27] a simple bifurcation analysis of the wave pinning model is carried out. In the same spirit, in [34] linear and weakly non-linear analysis of the Otsuji model is performed. Also [32] identify a cusp bifurcation as being the organising centre responsible for setting up the bistable kinetic profile responsible for the cell polarisation.

The aim of this paper is to consider the effect of source and loss terms on the wave-pinning model. Specifically we are motivated by the related Schnakenberg-like model proposed by Payne and Grierson [31] and further studied in [2, 3] for the formation of a single localised patch of active Rho's in *Arabidopsis* root hair cells. That model has striking similarities to the wave-pinning model, with the main difference being the presence of source and loss terms which were argued to represent nuclear control and secondary growth initiation processes respectively, which occur on a similar timescale to the the patch formation.

Specifically, in what follows, we shall study the dimensionless system of equations

$$\partial_t u = \delta \partial_{xx} u + [F(u,v) - \varepsilon\theta u], \tag{1a}$$

$$\partial_t v = \partial_{xx} v - [F(u,v) - \varepsilon\alpha], \qquad x \in [-L, L], \quad \partial_x(u,v)(\pm L) = 0, \tag{1b}$$

$$\text{where} \quad F(u,v) = \gamma \frac{u^2 v}{1+u^2} - \eta u + v. \tag{1c}$$

Here $2L \gg 1$ is a large (possibly infinite) domain length, $u(x,t)$ and $v(x,t)$ represent the concentrations of active and inactive species respectively and $\delta \ll 1$ is the ratio of their diffusion rates. The function $F(u,v)$ represents the local kinetics of the activation step parametrised by $\mathcal{O}(1)$ parameters η, γ. The specific form of F is not important and indeed we shall also consider a simpler form in section 3 in order to make explicit illustrative calculations. The parameters α and θ represent the strength of a constant source of inactive form and linear loss of active form respectively, with $\varepsilon > 0$ representing the relative importance of these effects compared to the other dynamics. In particular we shall be interested in both the cases $\varepsilon = 1$

and $\varepsilon \to 0$; the latter case leading precisely to the wave pinning model.

The rest of the paper is organised as follows. Section 2 contains a brief review of the biology of cell polarisation and of the minimal reaction-diffusion models that have been proposed to describe it. Then, section 3 contains a new, simplified analysis of the wave-pinning mechanism. Section 4 contains analytical, simulation and numerical continuation results on the existence of stable localised states of the model (1) for $\varepsilon = 1$, while taking δ and γ as bifurcation parameters and prototypical values of the other constants. Parameter regions are identified in which homogeneous states, periodic states, localised patterns, or isolated pulses may be observed. Then, the key question is addressed in section 5 of how this structure composed by different states collapses to the wave-pinned fronts solutions in the mass-conservation limit $\varepsilon \to 0$. First, numerical results show how the pulse solutions transform into front and back pairs with non-vanishing core and tails. These results suggest distinguished scalings that leads to a multiscale asymptotic analysis. This analysis also explains the key differences observed on a finite rather than infinite domain. Finally, section 6 draws conclusions and discusses potential implications of our findings to the biology of cell polarisation and more generally to pattern formation theory.

2. Cell polarisation models.

Eukaryotic cells can respond to gradients caused by small differences in concentration of exogenous or internal chemical signals. The phenomenon of cell polarisation induced by such stimuli has been observed experimentally in several cell types such as: budding yeast, *Dictyostelium discoideum* and Mammalian cells (white blood cells) [36]. From these experiments, many factors involved in the cell polarisation have been identified, a few being proteins like small GTPases (Cdc42, RaC and Rho), PI membrane lipids (PIP, PIP_2 and PIP_3) and Arp 2/3 (in active cytosol form). The interaction and spatial concentration of these factors depend on the cell-type, position and cellular state. Moreover, the molecular networks responsible for cell motility or chemotaxis are complex and depend on the cell-type. However, the basic mechanisms seemed to be preserved across all eukaryotic cells even though not all these factors are present in every cell type.

Consequently, in order to study cell polarisation as a phenomenon independent of cell-type, a minimal approach is often used, where the features that are common to all cell-types studied are captured. The most relevant factors appear to be the small GTPases, known collectively as Rho proteins. These proteins are present in the cytosol (in inactive GDP-bound form) and the membrane (in active GTP-bound form). There is a constant exchange between the active and inactive forms. The active form can be deactivated via GTPase activating proteins (GAPs) and the inactive forms can be activated by Guanine exchange factors (GEFs). GEFs are thought to be responsible for the observed positive feedback, or autocatalysis of the activation step. Moreover, experimental observations have shown that there is a big difference between the diffusion ratios of G-proteins in the membrane and the cytosol (Figure 1(c)). Finally, within the timescale of polarisation (minutes), the total amount of the protein (considering both active and inactive form) is often taken to be constant [14].

The spatio-temporal dynamics of the concentration of G-proteins in the cell (whether in active or inactive form) are determined by two processes: *diffusion* and *reaction*. The diffusion is responsible for the spatial dependence. On the other hand, GAPs and GEFs induce local reactions that are modelled typically by the non-linear interplay between components.

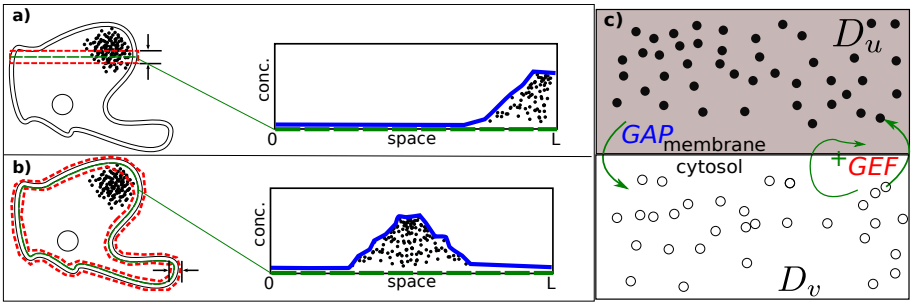

Figure 1. *Schematic description of the mathematical modelling. (a,b) Representation of the one-dimensional spatial domain as the limit (green line) when either a typical radial ((a), left)) or circumferential ((b), left) slice of the cell is considered (red dashed rectangle). Consequently polarisation corresponds to either a front solution ((a), right) or a localised solution ((b), right). (c) The modelled protein exists in an active form in the membrane, with diffusion constant D_u and the inactive form is in the cytosol (with active form D_v). The protein is deactivated by GAPs and activated through GEFs, the latter of which is assumed to be autocatalytic.*

In [26], the wave pinning model (expression (1) when $\varepsilon = 0$) was introduced as a minimal reaction-diffusion description for the cell polarisation problem. In their derivation, the one-dimensional domain is obtained from taking a typical radial slice through the cell. Throughout the spatial domain, both *cytosol* and *membrane* are present. In the Figure 1 a sketch of the domain is depicted. In this scenario, the cell polarity is characterised by increased concentration of active G-proteins (black dots in the Figure 1(c)). In the continuum limit, such a state would correspond to a front connecting low to high concentrations of the active form (Figure 1(a), right). Thus, the wave-pinning model considers the spatio-temporal dynamics of the concentration of a single G-protein, existing in active and inactive form in the same long spatial interval.

To explain where the model comes from, let $\hat{u}(\hat{x}, t^*)$ and $\hat{v}(\hat{x}, t^*)$ represent the concentrations of the active and inactive forms. Experimental findings show that there is at least a ten-fold difference between the diffusion rates of the active and inactive forms; in dimensional co-ordinates $D_u \ll D_v$. The conservation of total concentration suggests both the use of a non-flux boundary conditions and the same kinetic function $\hat{F}$ for creation of active and destruction of inactive forms. The function $\hat{F}$ accounts for both the activation and deactivation steps, mediated by the GEF and GAP respectively. Let k_0 and $\bar{\delta}$ represent the basal rates of each process. The positive feedback of the activation can be modelled by a *Hill function*, the simplest form of which should have coefficient 2, in order to enable the appropriate symmetry consideration. Letting the Hill parameters be given by γ and K^2, we have the simplest form

$$\hat{F}(\hat{u}, \hat{v}) = \gamma \frac{\hat{u}^2 \hat{v}}{K^2 + \hat{u}^2} - \bar{\delta}\hat{u} + k_0 \hat{v}.$$

Actually, as discussed and explored in [27], any reasonable function can be used, as long as it

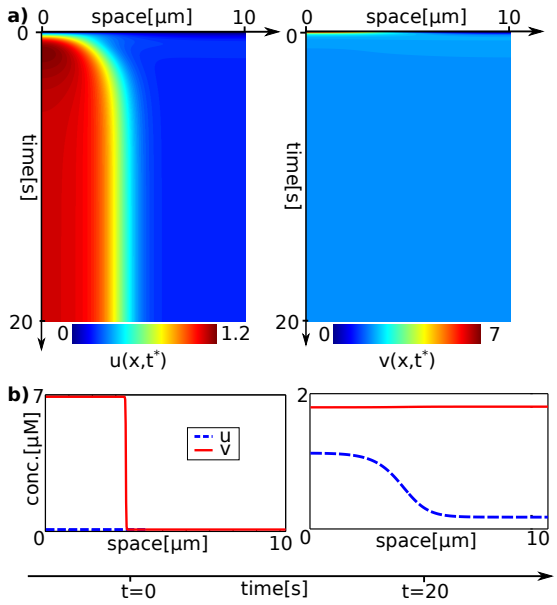

Figure 2. *Numerical observation of the wave-pinning phenomenon in model (2); (a) spatio-temporal plots, (b) initial and final solutions. See text for details. Parameter values are* $2L = 10[\mu m], \delta = 1[s^{-1}], \gamma = 1[s^{-1}], K = 1[\mu M], k_0 = 0.067[s^{-1}], D_u = 0.1[\mu m^2 s^{-1}], D_v = 10[\mu m^2 s^{-1}]$.

satisfies certain non-degeneracy assumptions. Given $\hat{F}$, the full model is

$$\partial_{t^*}\hat{u} = D_u \partial_{\bar{x}\bar{x}}\hat{u} + \hat{F}(\hat{u},\hat{v}), \tag{2a}$$

$$\partial_{t^*}\hat{v} = D_v \partial_{\bar{x}\bar{x}}\hat{v} - \hat{F}(\hat{u},\hat{v}), \qquad \bar{x} \in [-L, L], \quad \partial_{\hat{x}}(u,v)(\pm L) = 0, \tag{2b}$$

$$T = \int_{-L}^{L} (\hat{u} + \hat{v}) d\bar{x}. \tag{2c}$$

Here T is proportional to the total mass of G-proteins in the domain. Note, from the form of these equations and the no-flux boundary conditions that $\partial_t T = 0$, so that the total mass is conserved.

Figure 2 shows simulation results for the model at typical parameter values. Initially (b, left), an asymmetrical stimulus is applied for the inactive form v (continuous red line) while the active form u remains homogeneous (blue dashed line). Consequently, the active form $u(x,t)$ develops a front solution that propagates as the inactive form tends to a roughly homogeneous equilibrium (see the spatio-temporal plots in (a)). After a characteristic time, a steady front is established in the active form (cf. the dashed blue line in (b), right).

An in depth treatment of the wave-pinning model and its various extensions can be found in [26, 27]. An energetic explanation of the pinning phenomenon is given in section 3.

According to the theory developed in [33], a front connecting two given homogeneous equilibria will be stable only at one point in the parameter space called the *Maxwell point* (see section 3 for more details). In the case of model (2), it possess a continuum of homogeneous equilibria given by the curve $F(u,v) = 0$ which is the nullcline of both the u and v spatially-

independent systems (cf. Figure 3(a)). This degeneracy provides an extra degree of freedom in the system which turns the *Maxwell Point* into an interval of parameter values.

When an asymmetrical stimulus is applied to v and a monotonic front arises, then the homogeneous equilibria either side of the front are free to move along the nullcline $F = 0$, attaining a stable stationary front whose homogeneous equilibria lie in the *Maxwell Region*, a subset of the *bistability region*. The precise choice of which among the family of possible front solutions is chosen is determined by the initial total mass T.

In comparison with other proposed models, the wave pinning mechanism seems to account for several typical features of experimental observations (see [17] for a review). For instance: the polarisation time in the model ($\sim 20s$) is in good agreement with experiments, the homogeneous states are stable and the front can be reversed through the introduction of new stimuli. Due to its popularity, the wave pinning model has also served as a basis for further investigation of cell polarisation phenomena [38, 32].

It is useful to nondimensionalise the wave-pinning model by introducing the dimensionless quantities:

$$t = k_0 t^*, \; x = \bar{x}\sqrt{\frac{L^2 k_0}{D_v}} = \bar{x}\mathcal{L}, \; \delta = \frac{D_u}{D_v},$$

$$\gamma = \frac{\bar{\gamma}}{k_0}, \; \eta = \frac{\delta}{k_0}, \; \hat{u} = Ku, \; \hat{v} = Kv,$$

the model (2) takes the form

$$\partial_t u = \delta \partial_{xx} u + F(u, v), \tag{3a}$$

$$\partial_t v = \partial_{xx} v - F(u, v) \quad x \in [-\mathcal{L}, \mathcal{L}]\,, \tag{3b}$$

$$\text{where} \quad F(u, v) = \gamma \frac{u^2 v}{1 + u^2} - \eta u + v. \tag{3c}$$

We can break the mass conservation law by adding generic source and loss terms (as in [37]). The extra control parameter ε is introduced in order to investigate the role played by the new terms. The new extended model therefore takes the dimensionless form (1)

3. Energetic description of the wave-pinning phenomenon. The above-described phenomenon of wave pinning can be understood in terms of Maxwell-point theory as follows. Consider the dimensionless wave-pinning model (3) and introduce the new variables

$$R(x) = \delta u(x) + v(x), \quad S(x) = \delta u(x) - v(x).$$

The spatial system then takes the form

$$\frac{d^2 R}{dx^2} = 0, \tag{4a}$$

$$\frac{d^2 S}{dx^2} = -2F(S, R_*) := -\frac{dV}{dS}(S, R_*). \tag{4b}$$

Owing to the boundary conditions, the solution for the R variable is a constant, $R = R_*$ say. Hence the four-dimensional spatial dynamical system is reduced to a two-dimensional

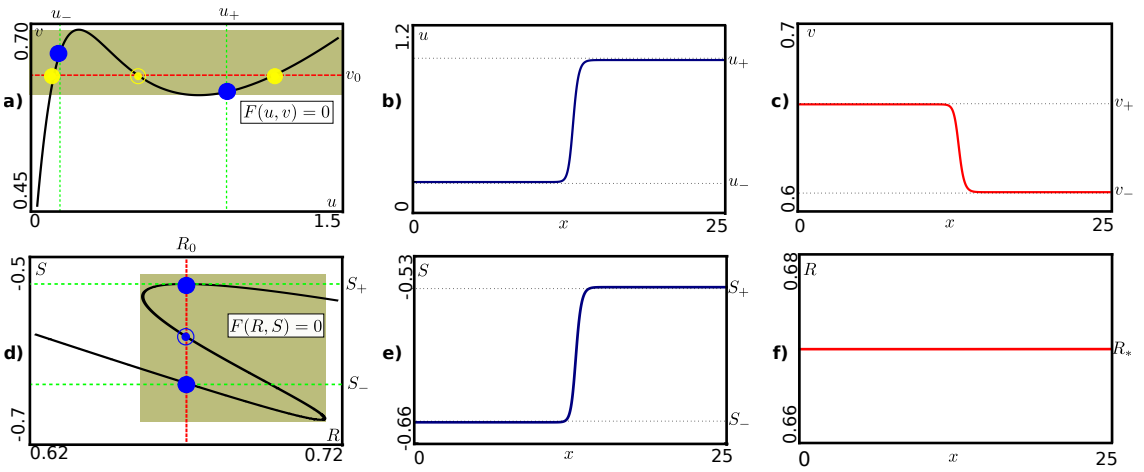

Figure 3. *Illustrating the wave pinning phenomenon in two different coordinates systems, see text for details. Parameters values used are* $\delta = 0.06$, $\gamma = 15$, $\eta = 5.2$, $2L = 25$.

one for the variable S, albeit with an unknown parameter R_*. This new formulation enables a simpler description of the wave-pinning phenomenon. In Figure 3, the panels (a) and (d) depict the nullclines in both the (u, v) and (R, S) coordinate systems, with the green areas demarcating the bistability region. Full and empty circles correspond to homogeneous equilibria that would be stable or unstable respectively in the absence of diffusion. Considering the front solution in the case $\delta \ll 1$, the changes in v along the front are negligible compared with the changes in u. Therefore, the inactive form is approximately constant ($v(x,t) \approx v_0$, note the small vertical scale in panel (c)). In Figure 3(a), the line solution for v_0 is depicted by a horizontal red dashed line. The yellow points correspond to the possible homogeneous equilibrium values for u when $v = v_0$. The blue points mark the values for (u_-, v_+) and (u_+, v_-) for the front solution. The components u and v are illustrated in (b) and (c). The corresponding pictures for the (R, S) coordinates are depicted in Figure 3(e,f). Here the front connects S_- with S_+ while $R = R_*$ is constant.

The right-hand side of equation (4b) can be seen as the derivative of a potential. Thus, the system conserves the energy given by

$$E = \frac{1}{2}\left(\frac{dS}{dx}\right)^2 + V(S, R_*). \tag{5}$$

Now, energy arguments can be used to construct solutions, because values of S that corresponds to minima of the potential $V(S, R_*)$, represent equilibria that are spatially stable. When both minima of the potential have the same value, the system is said to be at the Maxwell point [25]. Here, a heteroclinic cycle exists between the two equilibria. This solution represents a front solution (and its corresponding 'back'). We shall call the energy value at which such fronts and backs exist as $E = E_f$. Given E_f, it is possible to solve the differential equation (5) by separation of variables and obtain an implicit expression for the front solution

$$\int dx = x + C = \int \frac{dS}{\sqrt{2(E_f - V)}}. \tag{6}$$

The family of front solutions are parametrised by C, which represents the position of the core. Considering the kinetics given by (3c), for a certain values of parameters, the system (4b) has a Maxwell point and it posses three zeros S_-, S_m, S_+ (cf. Figure 4(a)).

Upon integration of the right-hand side of (4b), it is possible to obtain a closed-form expression for the potential

$$\begin{aligned} V(S,R_0) &= 2\int F(S,R_0)dS + V_0 \\ &= \frac{3\gamma\delta R_0^2 + 4\gamma\delta^2\left(\delta\log\left(4\delta^2+(R_0+S)^2\right) - 2R_0\,\mathrm{arccot}\left(\frac{2\delta}{R_0+S}\right)\right)}{2\delta} \\ &+ \frac{2R_0S(\gamma\delta+\delta-\eta) - S^2(\gamma\delta+\delta+\eta)}{2\delta} + V_0. \end{aligned}$$

The set of equienergetic curves (including the heteroclinic orbit) in the $(S, S_x)-$phase plane form the conservative phase portrait depicted in Figure 4(c). The numerical front solution is highlighted with a red dashed curve in the space and phase space in Figure 4(b) and (c) respectively. Even though this numerical solution satisfies expression (6), obtaining a closed-form expression is cumbersome. Instead we can consider p, a cubic polynomial approximation of F given by

$$F\left(w = \frac{R_* + S}{2\delta}\right) = F(w) = \frac{p(w)}{1+w^2},$$

$$p(w) = \frac{R_*}{w_+ w_- w_i}(w-w_i)(w-w_-)(w-w_+).$$

Where $w_\pm, w_i$ correspond to the maximum, minimum and intermediate zeros of p respectively and therefore $w_{\pm,i} = (R_* + S_{\pm,m})/(2\delta)$. In Figure 4(a), a comparison between F and p is depicted (red continuous and green dashed lines respectively). The cubic approximation p presents qualitatively the same behaviour as F. Considering p it is possible to solve (6) analytically and obtain a closed-form expression for the front

$$S(x) = S_- + \left(\frac{S_+ - S_-}{2}\right)\left(1 + \tanh[\xi(x-C)]\right), \tag{7a}$$

$$\xi = \left(\frac{S_+ - S_-}{4}\right)\sqrt{\frac{2R_*}{(R_*+S_-)(R_*+S_m)(R_*+S_+)}}. \tag{7b}$$

The expression (7a) captures the essential features of the front-like solution. In particular, (7a) provides an analytical approximation of the "width" of the front (Δ in Figure 4(b)). The values $x_\pm$ correspond approximately to the extreme values of the second spatial derivatives of (7a). The width of the front an its relation with the core position are given by

$$x_\pm = C \pm \frac{\Delta}{2}, \quad \Delta = \frac{2}{\xi}\mathrm{arcsinh}\left(\frac{1}{\sqrt{2}}\right). \tag{8}$$

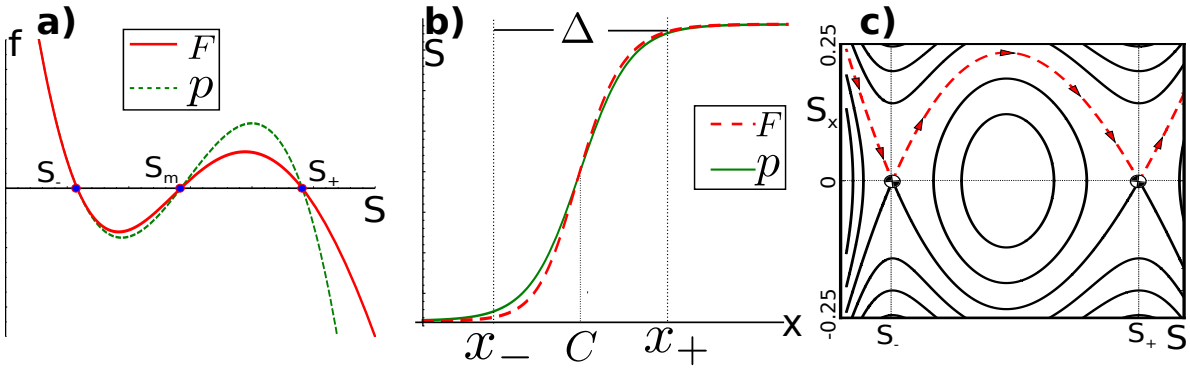

Figure 4. *Energetic description of wave pinning. (a) The function F in terms of the new variable S, and its cubic approximation p. (b) Graph of a front (heteroclinic) solutions; numerical solution of (4b) (dashed line) and analytical solution (7a) (solid line). (c) Phase space obtained from level sets of the energy E, with the dashed red line corresponding to the heteroclinic solution connecting S_- with S_+. Parameter values are:* $R_* = 1.849, \delta = 0.06, \gamma = 15, \eta = 15, S_- = -1.8273, S_m = -1.77756, S_+ = -1.71962$.

4. Localised states of the non-conservative system.

In this section we now consider an investigation of the dynamics of (1) in the case $\varepsilon = 1$. As a first remark, in contrast with the case where the mass is conserved, this new system posses a unique homogeneous equilibrium given by

$$(u_0, v_0) = \left(\frac{\alpha}{\theta}, \frac{\alpha(\varepsilon\theta + \eta)(\theta^2 + \alpha^2)}{\theta[\theta^2 + \alpha^2(1+\gamma)]}\right) = \left(\frac{\alpha}{\theta}, \beta_0 + \varepsilon\beta_1\right). \tag{9}$$

4.1. Linear and weakly non-linear stability analysis.

Performing a linear stability analysis around the homogeneous equilibrium, we can find the conditions for a pattern formation instability (also known as a Turing bifurcation or, in spatial dynamics as a Hamiltonian-Hopf bifurcation). Such bifurcations are of codimension-one in the parameter space, see e.g. [7, 28, 37]. To look for such bifurcations, we substitute the following ansatz into (1)

$$(u, v) = (u_0, v_0) + (\bar{u}, \bar{v})e^{ikx+\sigma t} \quad ||(\bar{u}, \bar{v})|| \ll 1, \tag{10}$$

neglect the non-linear terms for $(\bar{u}, \bar{v})$ and impose that the maximum of the real part of $\sigma(k)$ be zero. This then allows us to solve for the critical parameter value and predict the critical wavelength of the bifurcation. Proceeding in the usual way, we find the expressions for the critical point and the wavevector to be:

$$\varepsilon\theta\partial_v F - \frac{(\partial_u F - \delta\partial_v F - \varepsilon\theta)^2}{4\delta} = 0, \tag{11a}$$

$$k_c^2 = \frac{\partial_u F - \delta\partial_v F - \varepsilon\theta}{2\delta} > 0, \tag{11b}$$

where $\partial_\xi F = \left.\frac{\partial F}{\partial \xi}\right|_{(u_0,v_0)}$ when $\xi = u, v$.

We can understand the behaviour of the system in the vicinity of the spatial instability by introducing the change of variables

$$(u, v) = (u_0, v_0) + (U, V),$$

into (1) to obtain

$$\partial_t \begin{pmatrix} U \\ V \end{pmatrix} = [\mathbb{J} + \mathbb{D}\partial_{xx}]_c \begin{pmatrix} U \\ V \end{pmatrix} + \begin{pmatrix} 1 \\ -1 \end{pmatrix} \mathbb{NL}(U, V), \tag{12}$$

where $[\mathbb{J} + \mathbb{D}\partial_{xx}]_c$ is the linear operator evaluated at the critical point (evaluated at (9) and (11)), composed of the jacobian matrix $\mathbb{J}$ and the diagonal matrix accounting for the second spatial derivative $\mathbb{D}$. The scalar quantity $\mathbb{NL}$ corresponds to the nonlinear terms in the expansion.

If we assume the pattern to be a time-independent linear solution of (12), we obtain

$$\begin{pmatrix} U \\ V \end{pmatrix}_l = (Ae^{ik_c x} + \bar{A}e^{-ik_c x}) \begin{pmatrix} \partial_v F \\ -\partial_u F + \varepsilon\theta + k_c^2\delta \end{pmatrix}, \tag{13}$$

where A stands for the amplitude of the pattern. We are interested in finding an amplitude equation for A in a neighbourhood of the instability. This amplitude equation can also be thought of as the normal form of the spatial dynamical system (where x is thought of as a time-like variable), see [15]. The calculation of the coefficients of the normal form can be carried out using the procedure outlined in [13]. The calculation is lengthy but standard, and we relegate the details to the Appendix A, giving only the bare essentials here.

The change of variables and the amplitude equation obey the ansatz:

$$\begin{pmatrix} U \\ V \end{pmatrix} = W^{[1]} + W^{[2]} + \dots, \tag{14a}$$

$$\partial_t A = \partial_t A^{[1]} + \partial_t A^{[2]} + \dots, \tag{14b}$$

where the superscript accounts for the order in A. We can solve this equation at each order; for example, at first order we have:

$$\partial_t W^{[1]} = \partial_A W^{[1]} \partial_t A^{[1]} = [\mathbb{J} + \mathbb{D}\partial_{xx}] U^{[1]}.$$

The choice $\partial_t A^{[1]} = 0$ reduces this equation to a linear one and therefore we have

$$W^{[1]} = \begin{pmatrix} U \\ V \end{pmatrix}_l.$$

At second order we can choose $\partial_t A^{[2]} = 0$ as well. Actually this is possible for *every even order*. On the other hand, when dealing with odd powers, there will be *resonant terms* (terms which are proportional to (13), the vectors in the kernel of the linear operator (12)) on the right-hand-side of (12). In order to ensure that the problem at each odd order is solvable, we need to impose a *solvability condition* using the Fredholm Alternative theorem. In summary, we find an amplitude equation of the form

$$\partial_t A = \epsilon C_1 A + C_3 A|A|^2 + C_5 A|A|^4 + \mathcal{O}(|A|^6 A). \tag{15}$$

Here ϵ is an unfolding parameter that accounts for the parameter variation around the critical point. The constants C_i are obtained from the solvability conditions and are functions of the parameters evaluated at the bifurcation point. More details are given in the Appendix A.

In our study, the main purpose for computing the amplitude equation is to find where the bifurcation changes from being subcritical to supercritical. As argued in [37], sub-criticality of the Turing bifurcation is a necessary ingredient for the birth of localised structures in reaction diffusion systems. This such a transition point represents the nascence of a bistability region, where the homogeneous state coexists with the patterned one. That transition happens whenever C_3 changes sign in equation (15) .

Formally speaking, for the amplitude equation, we also need to check that $C_5 < 0$ in order to ensure the existence of a higher order coefficient which stabilises the amplitude equation. We have found evidence for this numerically.

Considering $C_3 = 0$ and (11a) as implicit functions of two of the system parameters, the nascence of bistability will thus occur at the codimension-two intersection point of both curves.

4.2. Numerical simulation results. The system (1) with $\varepsilon = 1$ has five parameters, and it is unfeasible to explore the effect of varying every possible combination. So, following [38, 26, 17], we fix all of them except two and consider the effect of variation only of the non-linearity in the system γ and the diffusion ratio δ. The fixed values of the other parameters will be taken to be

$$\varepsilon = 1, \quad \eta = 5.2, \quad \theta = 5.5, \quad \alpha = 1.5, \quad L = 100, \tag{16}$$

unless otherwise stated.

The left-hand panel of Figure 5 shows the basic bifurcation curves in the (δ, γ)-parameter plane, in a region where all the qualitatively different behaviours can be observed. The black continuous line corresponds to the spatial instability curve (equation (11a) when k_c^2 is positive in (11b)). This curve splits the parameter space into a region where just patterns are observed (above the line) and the rest. The dashed green line indicates where the cubic coefficient in the amplitude equation (15) vanishes. This curve is only relevant at its intersection with the spatial instability curve, at the light blue point. For values of δ smaller (greater) than the light blue point, a *sub-critical* (*super-critical*) bifurcation for the amplitude of the patterns takes place. The red dashed line in the lower part of the figure indicates where the dispersion relation [7] of the homogeneous states changes from having a maximum at zero (beneath this line) to have a non-zero maximum (above), the points in this curve correspond to a bifurcation which was termed a *Belyakov-Devaney* (BD) point in [5].

All the curves and points listed so far were obtained through analytic calculations. Moreover, the pink region corresponds to the region where localised structures were found using numerical continuation (the details will be explained below). Finally, the red dots are representative points in the parameter plane, where qualitatively different solutions are observed.

In order to explore the dynamics of model (1), we proceed to simulate the full PDE system using finite differences in space (with $dx = 0.01$) and fourth-order Runge-Kutta scheme in time (with fixed timesteps $dt = 10^{-3}$). Appealing to the Neumann boundary conditions, we also simulate on a half-interval $[0, L]$, with results on the full interval being obtainable by reflection in $x = 0$. Sweeping parameters and trying different initial conditions, it is possible to corroborate the predictions made by the linear stability analysis (subsection 4.1) and also find localised structures. The insets of Figure 5 on the right, depict the representative solutions.

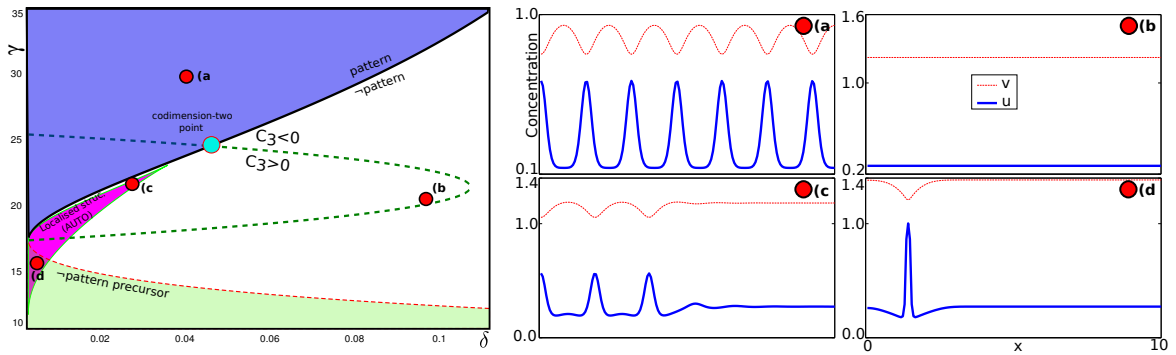

Figure 5. *Numerical two-parameter bifurcation diagram for the model (1) with fixed parameters (16) The pink shaded region is where localised solutions exist. The labelled points correspond to the qualitatively different stable equilibrium solutions illustrated in the corresponding sub-figures. The (δ, γ)-values depicted are: (a) periodic (Turing) pattern at $(0.0406, 30)$, (b) homogeneous equilibrium at $(0.10272, 20)$, (c) localised pattern at $(0.02688, 21.2411)$ and (d) a lone spike solution at $(0.002, 14.8)$.*

The solution in Figure 5(a) is a Turing pattern whose region of existence can be predicted using the critical condition (11). These patterns can be characterised in terms of their wavelength and amplitude which can be obtained using expressions (11b) and (15). Note how the oscillations of the active and inactive states are in anti-phase. These predictions are only valid in the vicinity of the instability. The homogeneous state observed in panel (b) is given by (9).

Further, the solution in Figure 5(c) corresponds to a localised patterned state, which when reflected onto the full domain $[-L, L]$ has five localised peaks of the active state (which correspond to troughs of the inactive state). In this parameter region we can find such localised patterns with an arbitrary number of peaks. Such solutions arise because there is a heteroclinic connection between the homogeneous state and the Turing patterns (as we shall explain shortly using the theory of homoclinic snaking). Note that there is a wavelength of the Turing patterns which corresponds to a well-defined distance between each of the peaks. These localised states coexist with the stable homogeneous, flat state. Sufficiently small initial conditions tend to converge to the flat solution whereas arbitrary sufficiently large initial conditions tend to converge to localised patterns with the numbers of peaks depending on the precise features of the initial data. On very long domains we can also find multiple localised patch patterns that are separated by long intervals of (almost) homogeneous solution.

The solution depicted in Figure 5(d) is also a localised solution, but is rather different. Here we see a single isolated peak (trough). This pattern has no underlying wavelength and the decay of the tails of the peak are monotonic rather than oscillatory. Here initial conditions are found to converge to either the stable homogeneous state or to just these single isolated peaks. If multi-peaked initial data is used, then over a short timescale, several well-separated peaks can be be formed. These peaks are then found to separate at a speed that decreases (exponentially) as the separation increases. Eventually, either the subsidiary peak is annihilated or it disappears to the edge of the domain, or, due to numerical noise a bound state can be formed consisting of two or more peaks separated by a large interval of homogeneous state. In fact, taking the mirror image of the solution in Figure 5(d) we would have just such

a "numerical" bound state.

Note that these two distinct kinds of localised solutions, either localised patterns with an underlying wavelength, or single isolated peaks are present in a broad spectrum of partial differential equations, derived in several different contexts; see section 6 for a discussion. In our case, a definite point of transition between the two behaviours can be identified (the red line in the lower region of Figure 5), which will be we explain in the next subsection.

4.3. Numerical continuation results. From the direct numerical simulations, it is possible to conclude that despite the system (3) not being variational, it does not present permanent dynamic behaviours such as limit cycles or chaos (at least not in the parameter regime under consideration). Therefore, we can focus our attention on time-independent solutions. This assumption reduces the partial differential equation to a reversible 4-dimensional systems of ordinary differential equations (ODEs), which can be studied using *spatial dynamics*, see e.g. [39]. Specifically, if $y(x) = (u, \partial_x u, v, \partial_x v)$ then we have

$$\partial_x \begin{pmatrix} y_1 \\ y_2 \\ y_3 \\ y_4 \end{pmatrix} = \begin{pmatrix} y_2 \\ \frac{\varepsilon u - F(y_1, y_3)}{\delta} \\ y_4 \\ F(y_1, y_3) - \varepsilon\alpha \end{pmatrix}. \tag{17}$$

Among the many advantages of studying the ODEs (17) instead of (1), is that the we can easily perform numerical continuation to look for periodic and localised solutions, for instance, using the software `AUTO` [9]. Numerical continuation allows us to unveil the region of existence, bifurcation and transition of the different solutions present in the system. Nonetheless, there are a few drawbacks. The continuation results do not give information on temporal stability, for that we need to study the full PDE system via simulation or spectral computation.

Taking the *localised pattern solution* from Figure 5(c) as a starting point for the continuation in γ, one obtains a sequence of solutions for the different values of γ. In order to visualise the continuation, it is useful to represent some one-dimensional quantity as a function of the parameter of continuation. One possibility is what we term $L_2 - Norm$ given by:

$$L_2 = \sqrt{\frac{1}{L}\int_0^L \sum_{j=0}^{4} y_j(x)^2 dx}.$$

In the Figure 6, curve shown following by the path is presented when the $L_2 - Norm$ is considered.

The most remarkable feature of this graph is the switching back and forth in a behaviour known as the *homoclinic snaking* [39, 4, 1, 3]. Within a certain region of the parameters, a family of solutions can be observed. Each one of these solutions exist in a line connecting two turning points, where a saddle-node bifurcation occurs. Hence, the two branches connecting any of these points have different stability. In order to determine the stability of each solution, we replace the different solutions in the full PDE (1) system and evaluate their persistence under perturbations. Here stable (unstable) solutions are represented by continuous (dashed) lines. Figure 6 also shows two different stable solutions that exist for the same value of γ.

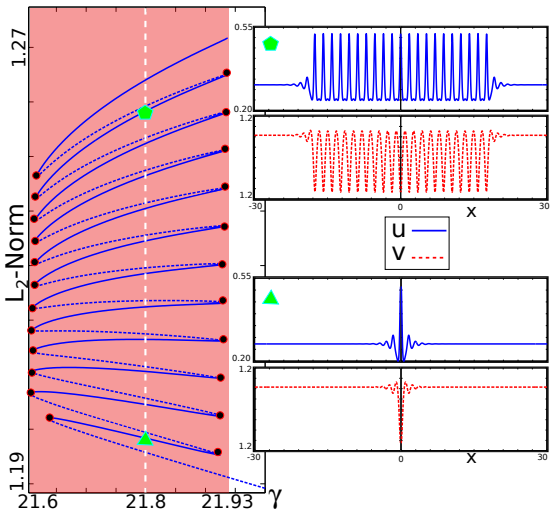

Figure 6. *Numerical continuation in γ of the localised pattern solution of (1) for $\delta = 0.02688$ and other parameters as in (16) $\eta = 5.2$, $\varepsilon = 1$, $\theta = 5.5$ and $\alpha = 1.5$. (Left) L_2-norm versus δ; dashed (continuous) lines represent unstable (stable) solutions. Each stable–unstable pair of solutions is connected through a saddle-node bifurcation marked by a black dot. (Right) Two distinct solutions for $\gamma = 21.8$ (marked by a triangle and a pentagon on the left-hand panel)*

Note that these solutions are left-right symmetric. According to the theory of snaking in non-variational systems (see [19]), there will be a bifurcation of a branch of non-symmetric states close to each saddle-node, but these will represent travelling rather than stationary states. Any stationary localised structure must be symmetric. The series of saddle-node bifurcations occur approximately at two values of γ, defining an interval known as the *snaking region* or *pinning region* where here pinning refers not to the front solutions of the wave-pinning model but to the pinning of the heteroclinic connection between the homogeneous state and Turing pattern. However, owing to the snaking region extending into the pulse region, we shall refer to the region as being the *localisation region*. The pink rectangle in Figure 6 represents the extent of the localisation region. Note that qualitatively similar results are obtained if we continue in δ rather than γ from the same initial localised state.

Using two-parameter continuation to trace the saddle-node points, it is possible to delineate the snaking region in the (δ, γ)-space. Tracking one fold at each edge of the snaking interval, we obtain two curves in the $(\delta, \gamma)-$space. The area delimited between these lines corresponds to the localisation region, which is also indicated in pink in the two-parameter plot in the left-hand panel of Figure 5,

In theory, we should expect the localisation region to extend all the way to the subcritical Turing bifurcation point. But note from Figure 6 that that the portion of the localised solution from the Turing bifurcation to the first fold is unstable. As we approach the codimension-two super-to-subcritical transition point, then, in accordance with theory [20, 19] the localisation region becomes an exponentially thin wedge which proceeds algebraically from the codimension-two point.

In practice, because of numerical precision and the finite domain effects (see [8]) the

numerical routine used to follow the saddle-nodes into the exponentially thin region breaks down. However the location of the (Maxwell) line in the centre of the localisation region can be easily located numerically.

The two-parameter plot reveals the richness presented by the family of localised solutions. In particular, both the spike and localised patterns solutions are both contained in the localisation region (see the left panel of Figure 5). In order to understand the mechanism of transition between these two kinds of state, we perform a one-parameter numerical continuation of the spike solution. The results are presented in Figure 7. In contrast with the localised patterns, for the spike solution continuation in δ and γ leads to qualitatively different results. As can be seen in Figure 5, the continuation of the spike solution in γ crosses the line which represents the BD transition, whereas continuation in δ does not cross this line.

According to linear stability analysis (cf. subsection 4.1), a homogeneous equilibrium will be linearly stable (linearly unstable) if the maximum of the real part of the dispersion relation $\sigma(k)$ is negative (positive). At zero, we are in the critical situation (e.g. (11) in our case). The dispersion relation can exhibit two qualitatively different behaviours, namely type I and III in the notation of [7], corresponding to the maximum for k being at zero and non-zero respectively (see Figure 7 (a) and (b)). In a stable regime ($\max(\sigma(k)) < 0$), any perturbations to the system will be decompose into Fourier modes with different wave numbers whose maximum is k, the *slowest* decaying mode. As a consequence, if we are in the case I, a non-zero wavelength will be observed during the transient dynamics that approaches the steady state solution. In this case it is said that there is the existence of a *pattern precursor*. On the other hand, a instability type III will not exhibit a precursor. Hence, in the left panel of Figure 5, the BD transition point corresponds to the point of transition between dispersion curves of type I and III. This transition curve can be determined analytically; in the case of (1), it corresponds to (11a) when (11b) is negative.

Figure 7(c) shows the continuation in δ. Here the saddle-node bifurcation corresponds to the right-hand limit of the localisation region, and connects the stable single spike solution to a lower-amplitude unstable single spike, as illustrated in the insets.

In contrast, Figure 7(d) shows continuation in γ. Here the solution crosses the BD line where the nature of $\sigma(k)$ changes from type I to type III. (cf. Figure 7(a) and (b)). In the absence of a pattern precursor (in the dark green shaded region) the solution is analogous to that with continuation in δ. Outside of this region, the spike solution develops oscillatory tails, and we are in the parameter region where we would expect to see homoclinic snaking. As part of the snaking scenario, the switching back through the right-hand saddle-node corresponds to where the solution acquires a new (symmetric pair of) localised peaks. As this new three-peak solution is traced back towards the BD point, the continuation fails to converge before reaching there. It is clear what happens is that the wavelength of the precursor tends to infinity as the BD point is approached and so the separation between the three peaks in the multi-peaked state also becomes infinitely large. Hence the branch of multi-peaked solutions disappears in a non-local bifurcation at the BD point. See section 6 for further discussion on this non-local bifurcation.

Thus we can see that the BD line splits the localisation region into two parts, the snaking region where localised patterns exist, and the region where there are only isolated spike solutions. Moreover, this observation is in complete accordance with the theory in [6] (and

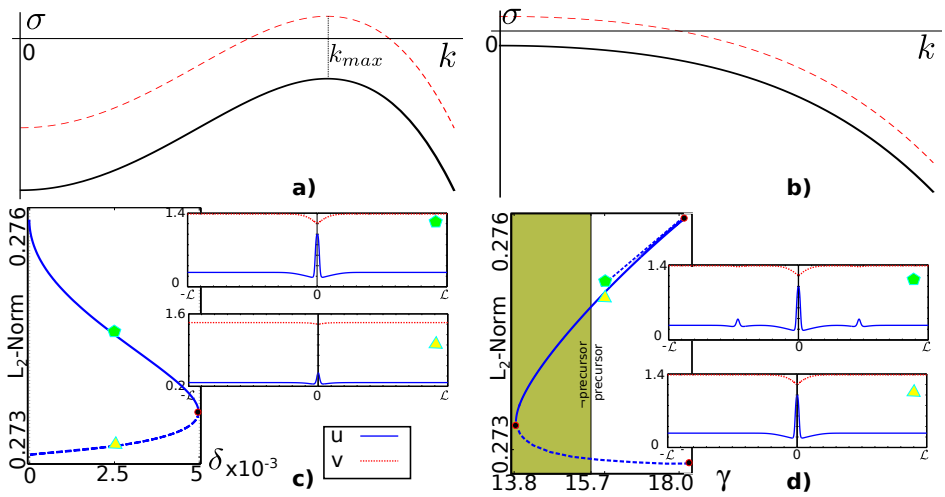

Figure 7. *(Top) Sketch of the dispersion relation $\sigma(k)$ for (a) type I and (b) type III. The dashed red (black continuous) curve corresponds to the unstable (stable) case. In* ***a)*** *$k_{max} \neq 0$ and therefore there is a precursor. (Bottom) One-parameter continuation results for the spike solution. When δ is varied (c), one saddle node bifurcation connects the large (stable) and small (unstable) solutions. When γ is varied (d), two saddle-nodes are observed. In the region where there is no pattern precursor (dark shaded panel), the saddle-node plays the same role as in (c). The second saddle-node connects to a branch of solutions with addition subsidiary peaks (different number of maxima), illustrated in the insets on the right.*

449 references therein), in which the existence of a spatial wavelength in the system is claimed to
450 be necessary ingredient for the existence of localised patterns.

451 **5. The mass-conservation limit $\varepsilon \to 0$.** So far we have been investigating how the wave-
452 pinning model changes when the mass is not conserved. Since in a realistic scenario the total
453 mass is *roughly* constant, we are interested in the case of small ε. From a mathematical
454 point of view, it is also intriguing to ask how the structure of localised and extended patterns
455 collapses to the wave-pinned solutions as we pass to the mass-conservation limit $\varepsilon \to 0$. In
456 particular, wave-pinning naturally leads to front solutions (heteroclinic orbits), a solution
457 where the spatial symmetry is broken, which can be argued to be a necessary ingredient for
458 cell polarisation. Indeed, when we run simulations for $\varepsilon = 0$, inhomogeneous initial conditions
459 on long domains quickly form a state with a number of fronts and backs which tend drift and
460 coarsen into a single wave-pinned front. For $\varepsilon = 1$, on the other hand, in the localisation region
461 inhomogeneous initial conditions on long domain quickly form states with a number of spikes
462 (or localised patterns) which slowly drift into either isolated spikes (or localised patterns).
463 We now seek to investigate how these two very different kinds of long term dynamics can be
464 connected as we vary ε from 1 and 0.
465 As a first step in understanding the mass-conservation limit, in Figure 8 we have plotted
466 the two critical curves where a Turing instability and a BD transition take place (given by the
467 analytic expressions (11a) when (11b) is positive and negative respectively), for a variety of
468 values of ε. Approaching the limit $\varepsilon \to 0$, we find that these two curves approach each other.
469 In fact it is possible to show that these curves become identical as $\varepsilon \to 0$.

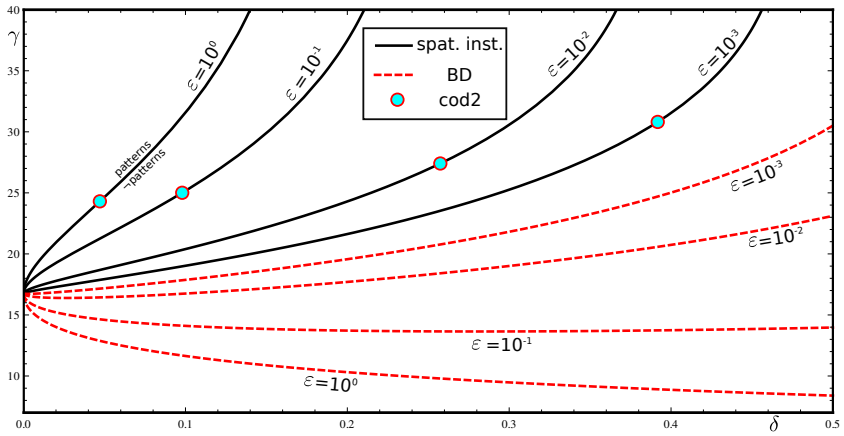

Figure 8. *Local bifurcation curves in the (δ, γ)-plane for different values of ε. The continuous black lines correspond to the Turing (spatial instability) bifurcation and the dashed red line to the BD transition point. In light blue the codimension-two point where the nascence of localised structures takes place.*

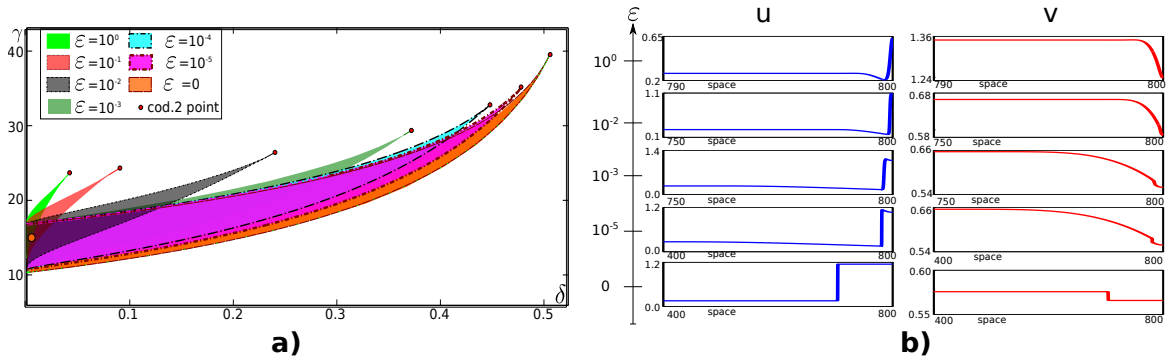

Figure 9. *(Left) comparison of the different localisation region as ε is varied. The red points correspond to the codimension-two super- to sub-critical Turing bifurcation transition point. Note the point identified in orange at $(\delta, \gamma) = (0.01, 16.8)$, which lies in the localisation region for all ε values depicted. (Right) Solution of the pulse solution at this point for different ε values, plot on the half-domain $[-L, 0]$. The parameter values are the same as in (16), except for $L = 800$.*

Hence, if any localisation region survives into the limit $\varepsilon \to 0$, the region of localised patterns will vanish, so that we are only left with localised spikes in the limit.

5.1. Numerical results. The natural next step is to compute, using the same procedure as in subsection 4.2, the localisation region for different values of ε. The results are presented in Figure 9. At first glance, notice how the localisation region grows as ε tends to zero. Hence, according to Figure 8, this region becomes increasingly composed of spikes rather than localised patterns. Interestingly, the intersection of this region with $\delta = 0$ seems to be independent of ε.

In order to compare the equivalent of the localisation region at $\varepsilon = 0$, we have delineated precisely the region in the two-parameter space where the wave-pinned fronts exist. Since the spatial dynamics of model (1) is singular at $\varepsilon = 0$, we can consider the equivalent 2-dimensional

problem obtained using the (R, S) variables (see equation (4) in section 3). Imposing the continuity between the different localisation regions, the extra parameter R_* in (4) is chosen such that $R_* = \lim_{\varepsilon\to 0} \delta u_0 + v_0$, where u_0, v_0 are given by (9). The codimension-two point at the tip of the region, which is calculated from the limit $\varepsilon \to 0$ in the analytical expression for C_3 in (15), gives a perfect prediction of the tip of the front region region obtained by two-parameter continuation. Moreover, although the localisation region grows significantly, it appears to vary continuously as ε is reduced to zero, with the upper and lower bounds of the front region continuing naturally into the upper and lower saddle-node bifurcations of the spike solutions for non-zero ε.

A next question is how localised spike solutions change their shape into being a *front*. Figure 9(b) illustrates how graphs of the solution are transformed as ε is reduced for fixed values of δ and γ. We start from the spike solution, in the middle of the domain, which we compute on the half-domain. As ε gets smaller, both components u and v start to develop a significant shelf so that the solution on the full domain resembles a front and back pair. Looking at just the u-component, we might imagine that the pulse converges uniformly to this front and back pair. Note also that, as expected, the exponential decay in the tail becomes progressively weaker.

However, there appears to be a subtlety. Looking at the penultimate solution, depicted for $\varepsilon = 10^{-5}$, we note that on the domain size depicted, although the decay rate of the tail gets weaker, its amplitude if anything (especially in the v-component) appears to grow. Also, the core of the pulse is not flat but appears to have a dimples in both u and v components. When comparing with the corresponding front solution at $\varepsilon = 0$, we see that the chosen left-hand limit of the solution is not the same as that of the front. Instead the non-vanishing weakly decaying tail seems to play the role of adjustment of the unique equilibrium values (u_0, v_0) for the pulse to the asymptotic values of the selected front of the wave-pinning model.

We therefore turn to asymptotic analysis to explore this curious phenomenon in the singular limit $\varepsilon \to 0$.

5.2. Asymptotic analysis. In the language of dynamical systems, the spike solution corresponds to a homoclinic orbit of the spatial system and the front solution to a heteroclinic one. Thus, considering the extended domain $[-L, L]$, the problem can be reformulated as the transition between a homoclinic solution whose maximum is at $x = 0$ and a heteroclinic loop. Since the solutions considered are even, the attention can be restricted to the domain $x \in [-L, 0]$. In section 3, we showed in the conservative case how the spatial dynamics can be reduced from a 4-dimensional space phase into a 2-dimensional one with a free parameter R_*. Hence, the transition involves a reduction of the number of degrees of freedom of the system as well as the nascence of a unique homogeneous equilibrium.

In order to study this transition, in the spirit of section 3, we rewrite the spatial system in terms of the (R, S) variables. We shall also remove the dependence of the homogeneous equilibrium (given by (9)) on ε. Specifically, let

$$u = \frac{R+S}{2\delta}, \quad v = \frac{R-S}{2} + \varepsilon\beta_1. \tag{18}$$

Defining

$$\beta_1 = \frac{\alpha(\theta^2+\alpha^2)}{\theta^2+\alpha^2(1+\gamma)}, \quad \psi(u^2) = \frac{\gamma u^2}{1+u^2} + 1,$$

and substituting the new variables (18) into the time-independent version of (1), we obtain

$$\frac{d^2R}{dx^2} = \varepsilon\left[\frac{\theta}{2\delta}(R+S) - \alpha\right], \tag{19a}$$

$$\frac{d^2S}{dx^2} = \varepsilon\left[\frac{\theta}{2\delta}(R+S) + \alpha - 2\beta_1\psi\left(\left(\frac{R+S}{2\delta}\right)^2\right)\right] - 2F\left(\frac{R+S}{2\delta}, \frac{R-S}{2}\right). \quad x \in]-L, 0]. \tag{19b}$$

We can study the transition on the new system (19) by performing one-parameter numerical continuation in ε. Our starting point is the is the half-homoclinic solution at the orange point in Figure 9, transformed in the new variables (18). We will start our analysis by considering the case of the semi-infinite domain, with solutions that are asymptote to the same homogeneous value as $x \to -\infty$. To that end, we shall choose L to be arbitrarily large (we shall consider finite-domain effects in the next subsection). Consequently, the front is developed in a small region of the space, making it difficult to visualise the dynamics for the different values of ε. It is then instructive to plot the solutions using the new scale

$$X = \sqrt{\varepsilon}x, \quad X \in]-\mathcal{L}, 0], \quad \mathcal{L} = \sqrt{\varepsilon}L. \tag{20}$$

In Figure 10(a), ten solutions for representative values of ε are superimposed using the new scale. The solutions are hardly distinguishable as $\varepsilon \to 0$. This is a consequence of the solutions converging to a well-defined limit.

Zooming into the solutions, we observe the appearance of a front-like behaviour in the S component (see the inset for S in Figure 10(b)). This front solution can be studied as a *interior layer* problem using *matched asymptotics* [18, 16]. In this framework, two dynamical regimes can be distinguished. An *inner* zone where the solution varies on the fast $\mathcal{O}(x)$ scale and an *outer* zone, where the solution varies in the slow $\mathcal{O}(X)$ (given by (20)) scale. In the case of an interior layer, the space can be divided into three zones, as indicated in Figure 10(c); two *outer* zones (I and III) divided by an *inner* zone (II).

Assuming Neumann boundary conditions in the extrema $x = -L, 0$ and imposing continuity of the solution in the transitions between inner and outer zones, the boundary conditions for each zone can be defined. In the Table 1, the zones and boundary conditions are summarised. Note that in the inner zone the value for $R = R_0$ is assumed as constant in accordance to the leading order equation (21) in which we obtain the conservative wave-pinning model.

For the outer regions we rewrite (19) using the scaling (20), the equations at each order in ε are as follows

$O(1)$:

$$F\left(\frac{R+S}{2\delta}, \frac{R-S}{2}\right) = O(\varepsilon) = 0, \tag{21}$$

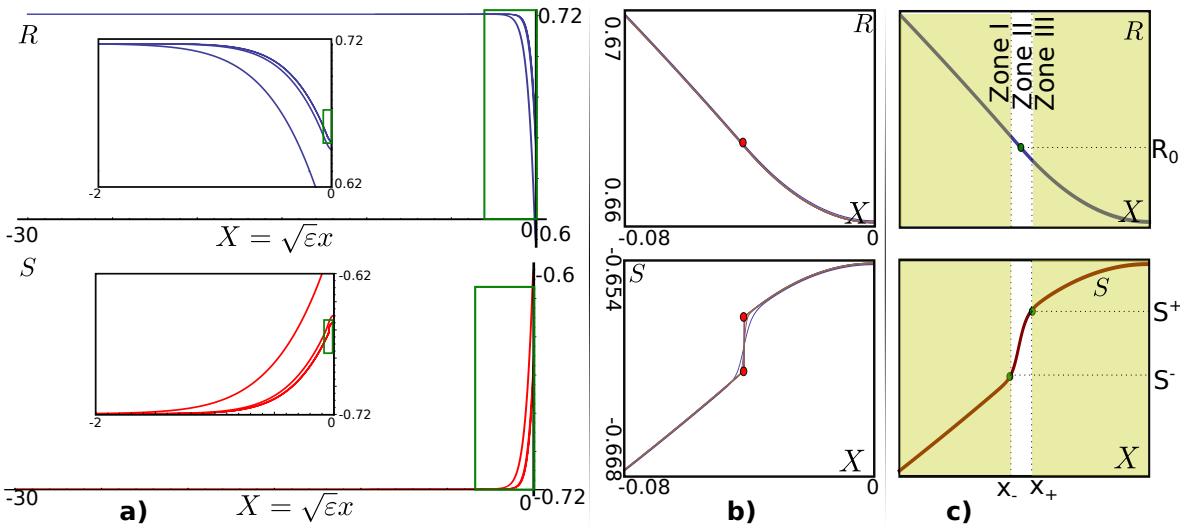

Figure 10. *Solutions of (19) in the half domain $[-L, 0]$ as ε tends to 0. The values of the parameters are: $\delta = 2 \times 10^{-3}, \gamma = 14, \eta = 5.2, \alpha = 1.5, \theta = 5.5, L = 10^5$. Superposition of the R (blue) and S (red) components of the homoclinic solution for $\varepsilon = \{10^{-n}\}_{n=0}^{9}$, the scaling $X = \sqrt{\varepsilon}x$ has being used in order to visualise all the solutions in the same plot. Zooms of the solution, highlighted in the green rectangle and shown in the insets. (b) Zoom around the front for both components. (c) Schematics of the behaviour for both components (see text for details).*

Zone	Interval	Boundary Conditions		regime
I	$x \in]-L, x_-]$	$\frac{d}{dx}(R,S)\|_{x=-L} = (0,0),$	$(R,S)\|_{x=x_-} = (R_0, S_-,)$	*outer*
II	$x \in [x_-, x_+]$	$(R,S)\|_{x_-} = (R_0, S_-),$	$(R,S)\|_{x_+} = (R_0, S_+)$	*inner*
III	$x \in [x_+, 0]$	$(R,S)\|_{x=x_+} = (R_0, S_+),$	$\frac{d}{dx}(R,S)\|_{x=0} = (0,0)$	*outer*

Table 1

Boundary conditions between the inner and outer regions. The interval for each region is specified using the original scale.

$O(\varepsilon)$:

$$\frac{d^2R}{dX^2} = \frac{\theta}{2\delta}(R+S) - \alpha, \tag{22a}$$

$$\frac{d^2S}{dX^2} = \frac{\theta}{2\delta}(R+S) + \alpha - 2\beta_1\psi + \chi(R,S). \tag{22b}$$

The separation of scale at $O(1)$ says that F is approximately zero, but there is an as yet unspecified contribution $O(\varepsilon)$. This contribution, termed $\chi(R,S)$, must be included at next order. In general χ depends on R and S and it can be seen as a Lagrange multiplier which makes the set of equations (21) and (22) a well-defined system of three differential-algebraic equations for the unknowns $R(X), S(X)$ and $\chi(R,S)$.

The boundary conditions Table 1 ensure the continuity of the solution, but they do not provide any information about the parameters involved in the asymptotics (namely, $R_0, S_\pm, x_\pm$).

More information can be extracted by imposing additional *matching conditions*. A natural matching condition for this problem is to impose continuity of the derivatives

$$\frac{d}{dX}(R,S)\bigg|_{x=x_-} = \frac{d}{dX}(R,S)\bigg|_{x=x_+}, \tag{23}$$

which can be sen as being necessary in the limit $\varepsilon \to 0$ in order to satisfy the appropriate jump condition across the inner zone that are consistent with the second derivative operator.

In summary, the transition under study is equivalent to the *interior layer* problem, which is given by: the boundary value problems of the inner region (19) and outer regions ((21) and (22)), the boundary conditions (specified in Table 1) and the matching condition (23).

In the remainder of this section, by making additional approximations to this problem, we will show how an analytical close-form approximate solution can be obtained. We will reduce the number of unknown parameters to just R_0.

First, since in the inner zone II the dynamics is driven by the leading order, we will consider this boundary value problem as equivalent to the conservative case and therefore the solution (7a) is an approximate analytical solution. The problem is then reduce to two outer problems (equations (21) and (22)) for zones I and III, whose solutions are given by (R_1, S_1) and (R_3, S_3) respectively. Under this assumption and considering the boundary conditions, the solution in S presents a discontinuity at the point $X = X^*$, which connects both outer zones. This assumption is equivalent to saying

$$X_- = X_+ = X^*.$$

When F is given by (3c), we can write the condition (21) in terms of the original variables (u, v) and obtain an analytical expression for $v(u)$. Expanding it up to linear order around a certain point $\hat{u}$, we obtain

$$v(u) = \frac{\eta u(1+u^2)}{1+u^2(1+\gamma)} \approx v(\hat{u}) + v'(\hat{u})(u-\hat{u}). \tag{24}$$

Replacing $u(R,S), v(R,S)$ by:

$$u = \frac{R+S}{2\delta}, \quad v = \frac{R-S}{2},$$

and substituting into (24), we can solve for $S(R)$ and then replace it into (22a), obtaining a second-order affine differential equation. The expressions for $S(R)$ and $R(X)$ thus obtained can be written

$$S(R) = \left(\frac{\delta - v'(\hat{u})}{\delta + v'(\hat{u})}\right) R + \frac{2\delta(\hat{u}v'(\hat{u}) - v(\hat{u}))}{\delta + v'(\hat{u})}, \tag{25a}$$

$$R(X) = Ae^{\sqrt{\frac{\theta}{\delta+v'(\hat{u})}}X} + Be^{-\sqrt{\frac{\theta}{\delta+v'(\hat{u})}}X} + v(\hat{u}) + \frac{\alpha\delta}{\theta} + v'(\hat{u})\left(\frac{\alpha}{\theta} - \hat{u}\right), \tag{25b}$$

where A and B are constants to be determined using the boundary conditions. Choosing for Zones I and III $\hat{u} = u_0 = \alpha/\theta$ and $\hat{u} = u_+ = (R_0 + S_+)/(2\delta)$ respectively and using the aforementioned boundary conditions, an analytic approximation for the domain composed by the two outer problems is

$$R(X) = \begin{cases} R_1(X) = \zeta(u_0) + (R_0 - \zeta(u_0))\,\frac{\cosh(\sigma(u_0)(X+\mathcal{L}))}{\cosh(\sigma(u_0)(X^*+\mathcal{L}))} & X \in [-\mathcal{L}, X^*], \\ R_3(X) = \zeta(u_+) + (R_0 - \zeta(u_+))\frac{\cosh(\sigma(u_+)x)}{\cosh(\sigma(u_+)X^*)} & X \in [X^*, 0] \end{cases} \tag{26a}$$

and

$$S(X) = \begin{cases} \varphi_1(u_0)R_1(X) + \varphi_0(u_0) & X \in [-\mathcal{L}, X^*], \\ \varphi_1(u_+)R_3(X) + \varphi_0(u_+) & X \in [X^*, 0]. \end{cases} \tag{26b}$$

Where

$$\zeta(u) = v(u) + \frac{\alpha\delta}{\theta} + v'(u)\left(\frac{\alpha}{\theta} - u\right), \qquad \sigma(u) = \sqrt{\frac{\theta}{\delta + v'(u)}},$$

$$\varphi_1(u) = \frac{\delta - v'(u)}{\delta + v'(u)}, \qquad \varphi_0(u) = \frac{2\delta(uv'(u) - v(u))}{\delta + v'(u)}.$$

This solution depends on the parameters $\{R_0, S_\pm, X^*\}$. Nevertheless, given R_0 we can find $S_\pm$ through (21). Moreover, when the dependence between R and S is linear (25a), the matching condition (23) is reduced to just the R component $R_1'(X)|_{X^*} = R_3'(X)|_{X^*}$. Replacing these expressions from (26a) we obtain:

$$\frac{(R_0 - \zeta(u_0))\sigma(u_0)}{(r_0 - \zeta(u_+))\sigma(u_+)} = \frac{\tanh(\sigma(u_+)X^*)}{\tanh(\sigma(u_0)(X^* + \mathcal{L})}.$$

Additionally, approximating $\tanh(\sigma(u_0)(X * +\mathcal{L})) \approx 1$ and $\tanh(\sigma(u_+)X^*) \approx \sigma(u_+)X^*$, the condition is reduced to:

$$X^* = \frac{\sigma(u_0)(R_0 - \zeta(u_0))}{\sigma(u_+)^2(R_0 - \zeta(u_+))}. \tag{27}$$

The set of equations (26) and (27) is an analytic approximation which is in good agreement with the numerical solution when R_0 is provided (see Figure 12). However, as a consequence of assuming a linear dependence between R and S, the matching conditions for each component (23) becomes linearly dependent and therefore the matching condition for S is satisfied trivially. Therefore, we are unable to determine R_0 using this method. We conjecture that a more accurate matching condition between the Zones I and III is required in order to uniquely determine R_0.

In what follows then, we have resorted to numerics to find R_0. Numerically, R_0 corresponds to the value of R at X^*, which corresponds to the minimum of R'. Using this method, in

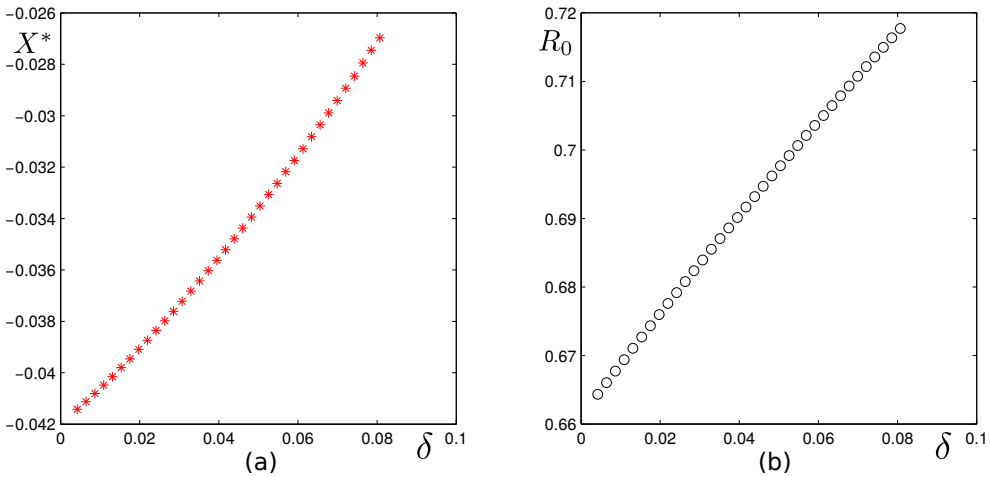

Figure 11. *Numerical determination of the asymptotic key quantities X^* (a) and R_0 (b) in (19) as a function of δ, when $\varepsilon = 10^{-5}, \gamma = 14, \eta = 5.2, \theta = 5.5, \alpha = 1.5, L = 10^3$.*

Figure 11 we depicted the determined values of R_0 and X_* for a range of values of δ when the system is in the quasi-conservative regime ($\varepsilon \ll 1$). The rest of the parameters have been specified in the caption. From this figure we can appreciate how the values for R_0, X^* vary continuously with the parameter and therefore they are well-defined.

In the Figure 12 (a), we have plotted the numerical solution (points) superimposed on the analytical (line) when R_0 is provided. The solution is illustrated for Zones I and III, for the R component. The same comparison for S can be obtained from R through (25a).

In Figure 12(b), the difference between the numerical and the analytical solutions is depicted as a function of ε . The value of Δ is given by:

$$\Delta = \int_{-L}^{x^-} |R_1(x) - R_n(x)| + |S_1(x) - S_n(x)|dx + \int_{x_+}^{0} |R_3(x) - R_n(x)| + |S_3(x) - S_n(x)|dx,$$

where the subscripts $1, 3, n$ stand for Zones I, III and the numerical solutions respectively. Moreover, as the limit is reached, the values of R_0 and X^* (the midpoint between x_+ and x_- in the ε-independent scale) attain quickly an almost constant value as ε tends to zero (cf. Figure 12 (c) and (d).

Given $x^* = X^*/\sqrt{\varepsilon}$, we can find numerically $x^{\pm}$ whether using (8) or by defining x^+ (x^-) as the first point to the right (to the left) of x^*, where the numerical solution (R, S) vanishes when is replaced into (21). From the numerical values of $x_\pm$ it is possible to measure the length of Zones I and III for several values of ε. In Figure 13 (a) and (b), the $\log - \log$ plot of the length as function of ε is presented for both zones. The points show a linear behaviour whose slope is approximate $-1/2$, which is in good agreement with our assumption for the scaling (20). Moreover, Figure 13(c) depicts a comparison between the function $v(u)$ (black continuous line) and the linear approximation (dashed green line) around the two values of $\hat{u} = u_0, u_+$. This figure illustrates how reliable our linear approximation is to $v(u)$ in Zones I

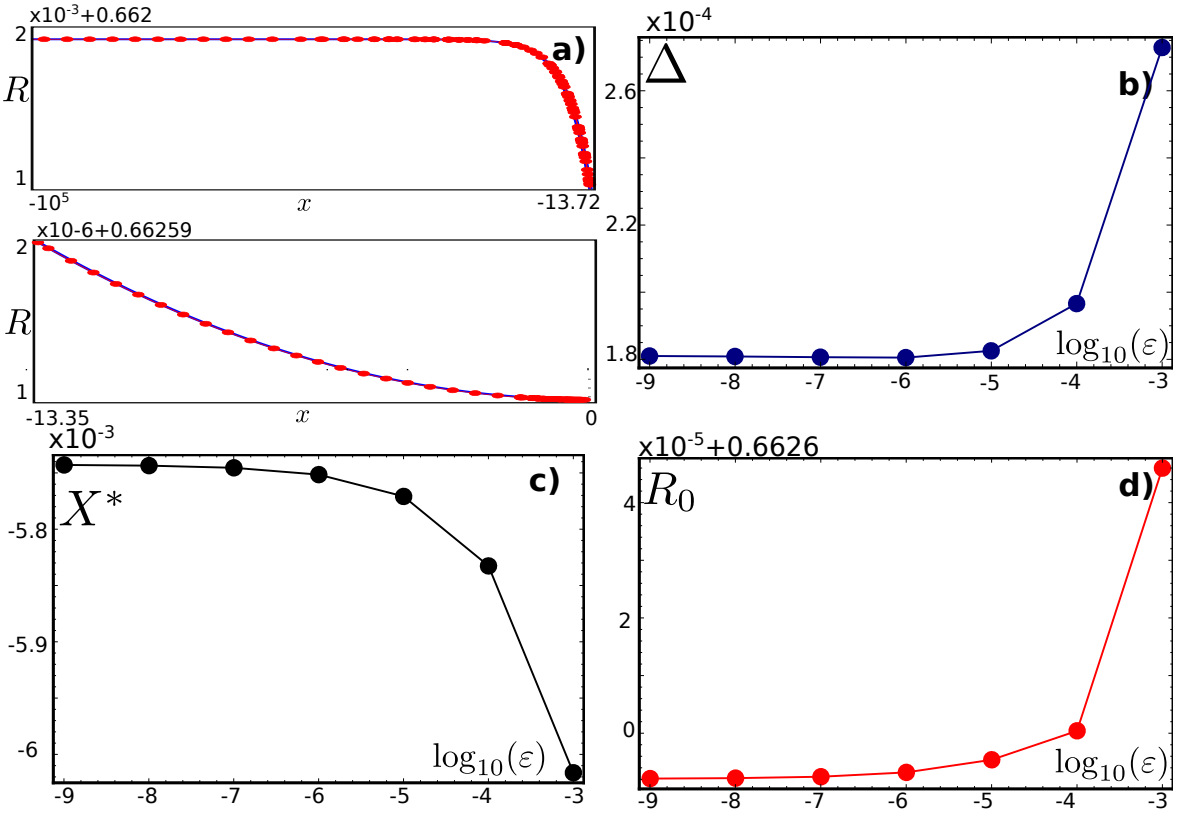

Figure 12. *Summarising the asymptotic approximation in the case of a given R_0. (a) comparison between the analytical (continuous line) and the numerical solution (red points) of R when $\varepsilon = 10^{-9}$, upper and lower plots correspond to Zones I and III respectively. (b) Difference between the analytical approximation (given by (26) and (27)) and numerical solutions as a function of ε. (c) Numerical value of the position of X^* as a function of ε. Numerical value of R in Zone II as a function of ε. The values of the parameters used are $\delta = 2 \times 10^{-3}, \gamma = 14, \eta = 5.2, \theta = 6, \alpha = 1.13$.*

and III.

5.3. Finite domain effects. So far we have been dealing with a domain that is large enough for all ε-values considered, that the localised solution can reach the homogeneous equilibrium at the left-hand boundary (essentially, an infinite domain). In the conservative case (cf. section 2 and references therein) the front selection is a property of the total mass, which itself is greatly affected by the length of the domain. Hence, a description of the transition to the finite-length case is highly relevant.

Taking the limit $\varepsilon \to 0$ in (26), we obtain the conservative solution (7). In contrast, the asymptotic analysis for a long domain showed a slowly varying behaviour in the outer zones, with the amplitude (but not the rate) of the variation being essentially independent the value of ε. This analysis implicitly assumes that Zones I and III can grow to become infinitely long, under the scaling (20) as $\varepsilon \to 0$. Therefore, for a small enough value of $\mathcal{L} = \sqrt{\varepsilon} L$, size effects will destroy this picture and the description provided by (26) will no longer apply.

The analytical solution (26) relies on the existence of a front solution for S which connects

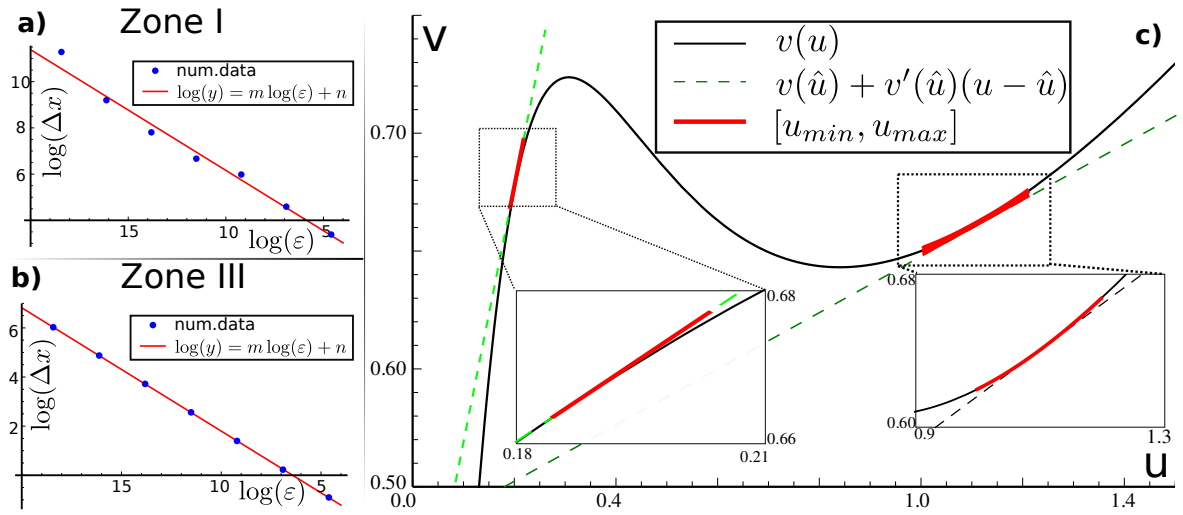

Figure 13. *(a) Size of Zone I as a function for ε (blue dots), the continuous line correspond to the linear fit: $m = -0.522$, $n = 0.934$. (b) Size of Zone III as a function for ε (blue dots); the continuous line correspond to the linear fit: $m = -0.502$, $n = -3.225$. (c) Superposition of $v(u)$ using (24) and the linear approximation around $\hat{u}$ (green dashed line). The range where u varies throughout the zone is highlighted in thick red. The approximation on the left (right) corresponds to $\hat{u} = u_0$ ($\hat{u} = u_+$). The values of the parameters used are $\delta = 2 \times 10^{-3}, \gamma = 14, \eta = 5.2, \varepsilon = 10^{-9}, \theta = 6, \alpha = 1.138$.*

$S_\pm$ at $x_\pm$ while $R = R_0$ remains constant (Zone II). Beyond that point (Zones I and III), the solution presents a slow exponential-like behaviour whose exponents are proportional to $\sqrt{\varepsilon}$. Finally, at the borders, the derivatives of the solution must vanish. It must be underlined that our approximate solution (26) does not have any link with the homogeneous value at $x = -L$.

Thus, whenever size effects are important, the solution at the left border assumes a different value from the homogeneous equilibrium and eventually reaches $S = S_-$ and $R = R_0$ as $\varepsilon \to 0$. Zone III will increases its size until it is affected by the finite size effect of Zone I. At $x = 0$, the value of the solution diminishes (increases) in the S (R) component until it reaches S_+ (R_0). Through this process, the limit solution (26) becomes precisely the front solution without the slowly varying inner core or tail. As a final remark, this description explains how the homogeneous value at $x = -L$ in the case $\varepsilon = 0$ can depend on the length of the domain.

In the Figure 14, the above described transition is illustrated for the finite value $L = 30$. When $\varepsilon = 1$ (highest and smallest values of R and S respectively in Figure 14(a) and (b)), the solution corresponds to a homoclinic orbit (depicted in half of the domain). As ε is diminished, the exponential-like behaviour in Zone I decreases its exponent according to (26). On the other hand, due to the size restriction and the boundary conditions, the values of the components change as $(R(x), S(x))_{x=-L} \to (R_0, S_-)$. Moreover, for a certain value of ε (in this case $\varepsilon \approx 10^{-3}$) the $S-$component becomes a pure front (see the black frame region in Figure 14(b)). When the front is established, Zone III can be distinguished and further decreasing of ε will displace the front to the left, increasing the size of Zone III while $(R(x), S(x))_{x=0} \to (R_0, S_+)$. Eventually the front stops its drift, due to the conservation of the total mass ((2c)). In Figure 14, we can observe how the solutions converge to a front for the S component and a

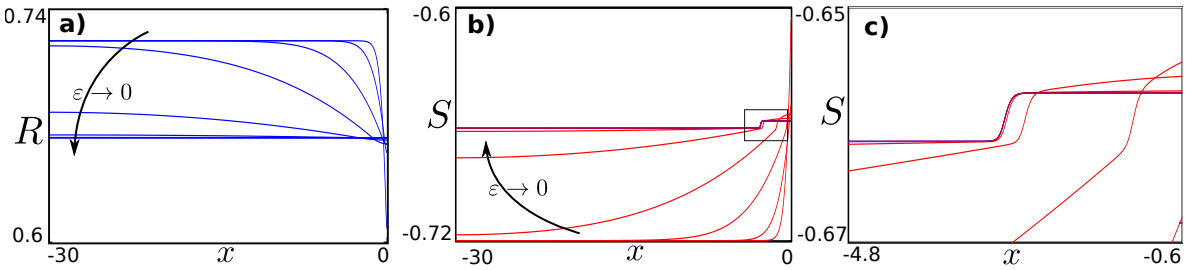

Figure 14. *Effect of domain size on the homoclinic to heteroclinic transition as $\varepsilon \to 0$, showing the (a) the R-component and (b) the S component, in the latter case illustrating the inner zone where the front develops. (c) A zoom of (b). The values of the parameters used are $\delta = 2 \times 10^{-3}, \gamma = 14, \eta = 5.2, \alpha = 1.5, \theta = 5.5$, $\varepsilon = \{0\} \cup \{10^{-n}\}_{n=0}^{10}$.*

homogeneous solution for R. The last solution corresponds to $\varepsilon = 0$.

6. Conclusion. The results of this investigation can be collected into three main conclusions

First, we studied the *wave pinning* model, a popular proposed mechanism for cell polarisation. By introducing the new (R, S) coordinates we have added a simpler explanation of how the wave-pinning works from a mathematical point of view. Specifically we can then see that the four-dimensional spatial system is essentially degenerate in that it can be represented as a two-dimensional systems with a free parameter R_*. This enables a simple mechanical analogy, the identification of a Maxwell region and an expression for the front solution in closed form up to quadrature for any local kinetic function F that has a bistable character. In certain special cases, an analytic function for the front can be obtained.

Second, motivated by biological systems where there is production and recycling of G-proteins, we have studied the effects of when the mass conservation present in the original wave-pinning model is relaxed. The addition of generic *source* and *loss* terms give rise to several equilibrium solutions such as homogeneous equilibria, periodic patterns, localised patterns, and isolated spikes. Moreover, through a combination of linear stability analysis and numerical continuation we have been able to delineate how these states are organised in a two-parameter diagram as the diffusion ratio and nonlinear driving parameter are varied, which relies on the theory of so-called homoclinic snaking. Within this analysis we identified the importance of a codimension-two bifurcation at which the pattern formation (or Turing) bifurcation changes from sub- to super-critical and the existence of what we have termed a Belyakov-Devaney transition in which the pattern precursor is lost.

Finally, we have studied the crucial question of how these two very distinct kinds of behaviour relate to each other by taking the limit $\varepsilon \to 0$, in which the source and loss terms disappear. We have shown how the so-called *localisation region* becomes filled with spike solutions and the localised pattern states disappear. Moreover we have highlighted the delicate asymptotics of how these spike solutions morph into wave-pinned fronts. In particular this has involved multiple-scale asymptotic analysis, in which there are three zones, two outer zones and an inner one. It is only within the inner zone that the front solution appears. The behaviour in the outer zones is more subtle and depends crucially on the domain size.

It might also be interesting to make some more general remarks about the implication of these results. Although the model under study is inspired by the phenomenon of cell polarisation, the mathematical findings in this manuscript might be relevant beyond this context. The model (1) is a reaction-diffusion system which accounts for a broad spectrum of phenomena. On the other hand, similar models to (1) have been proposed in a rather different context such as Rho proteins of plants (ROP) (for example [31, 2]). We think that the general analysis performed could shed light on the particular contexts where models similar to (1) are used to describe the dynamics.

The analysis we have presented, intended to be general and is independent of the specific form of the local kinetics embodied in the function F. We have simply used the specific expression (3c) in order to illustrate the analysis. More generally, a particular result we have found is the way that the BD transition causes a non-local bifurcation between localised pattern solutions and spike solutions. In effect, the homoclinic snake is annihilated by the BD transition through the additional peaks disappearing to the edge of the domain. Given that both types of localised structures exist in several context, this transition must be somehow universal. Actually, through private communications, we have learnt that this transition takes place in models that have similar properties to (1) that arise in: ecological systems [40], optical systems [30] and in a crime wave model [21]. A complete description of the non-local bifurcation and how it organises localised pattern to spike transition will form the subject of future work.

There also remain open questions regarding the asymptotic analysis of subsection 5.2. In that study, we fixed all the parameters except ε. In particular we fixed $\delta \sim 10^{-3}$. Moreover, a necessary ingredient for observing non-homogeneous solutions is to consider a small value of δ (see [27], where the asymptotic treatment is performed in the limit $\delta \ll 1$). Actually, when we studied the conservative case in section 3, we found an analytical approximation for the front (7a), whose width Δ (cf. (8)) depends on δ. Therefore, the asymptotic analysis for the transition of subsection 5.2, must be carried out considering both $\delta, \varepsilon \ll 1$. This is the next natural step in a better characterisation of this phenomenon, which may lead to a combination of singular perturbation theory with the multiple scales asymptotics studied here. It may indeed be possible to use some of the methods from geometric singular perturbation theory to make rigorous statements on the existence of localised solutions in this limit (see [10, 11] and references therein).

It should also be pointed out that we have not dealt with the stability of all of these solutions in the full PDE system in a systematic way. Instead we have relied on the persistence of these solutions observed in the numerical simulations of the PDE. An analytical treatment of the interaction of the fronts involved in the heteroclinic loop will be part of future work.

As a final conclusion, it is interesting to note that our analysis suggests that there is no real distinction between the Turing mechanism, wave-pinning or homoclinic snaking as pattern formation mechanisms in systems of reaction diffusion equations. In fully parametrised models, each can be seen as different explanations that are valid in a different distinguished limits. In a sense, they are like three sides of the same coin.

Acknowledgements. The authors acknowledge helpful conversations with Veronica Grieniensen, Stan Maree, John King, Michael Ward, Lendert Gelens, Yuval Zelnik, Marcel G. Clerc

and Rutuja Patwardhan. N. Verschueren would like to acknowledge “Programa de doctorado en el Extranjero Becas Chile Contract No.72130186.”

REFERENCES

[1] M. Beck, J. Knobloch, D.J.B. Lloyd, B. Sandstede, and T. Wagenknecht. Snakes, ladders, and isolas of localized patterns. *SIAM Journal on Mathematical Analysis*, 41:936–972, 2009.

[2] V. Breña–Medina, A.R. Champneys, C. Grierson, and M.J. Ward. Mathematical modeling of plant root hair initiation: Dynamics of localized patches. *SIAM Journal on Applied Dynamical Systems*, 13:210–248, 2014.

[3] V.F. Breña–Medina, D. Avitabile, A.R. Champneys, and M.J. Ward. Stripe to spot transition in a plant root hair initiation model. *SIAM Journal on Applied Mathematics*, 75:1090–1119, 2015.

[4] J. Burke and E. Knobloch. Snakes and ladders: Localized states in the Swift–Hohenberg equation. *Physics Letters A*, 360:681–688, 2006.

[5] A.R. Champneys. Homoclinic orbits in reversible systems and their applications in mechanics, fluids and optics. *Physica D: Nonlinear Phenomena*, 112:158 – 186, 1998.

[6] M.G. Clerc and C. Falcon. Localized patterns and hole solutions in one-dimensional extended systems. *Physica A: Statistical Mechanics and its Applications*, 356:48 – 53, 2005.

[7] M.C. Cross and P.C. Hohenberg. Pattern formation outside of equilibrium. *Rev. Mod. Phys.*, 65:851–1112, 1993.

[8] J.H.P. Dawes. Modulated and localised states in a finite domain. *SIAM J. Appl. Dyn. Syst.*, 8(3):909–930, 2009.

[9] E.J. Doedel, A.R Champneys, T.F. Fairgrieve, Yu.A. Kuznetsov, B. Sandstede, and X. Wang. Auto 97: Continuation and bifurcation software for ordinary differential equations (with homcont), 2002. Technical report, Concordia University.

[10] Arjen Doelman, Tasso J Kaper, and Paul A Zegeling. Pattern formation in the one-dimensional gray - scott model. *Nonlinearity*, 10(2):523, 1997.

[11] Arjen Doelman and Frits Veerman. An explicit theory for pulses in two component, singularly perturbed, reaction–diffusion equations. *Journal of Dynamics and Differential Equations*, 27(3):555–595, 2015.

[12] L. Edelstein-Keshet, W.R. Holmes, M. Zajac, and M. Dutot. From simple to detailed models for cell polarization. *Philosophical Transactions of the Royal Society of London B: Biological Sciences*, 368, 2013.

[13] C. Elphick, E. Tirapegui, M.E. Brachet, Coullet P., and G. Iooss. A simple global characterization for normal forms of singular vector fields. *Physica D: Nonlinear Phenomena*, 29:95 – 127, 1987.

[14] S. Etienne-Manneville and A. Hall. Rho gtpases in cell biology. *Nature*, 420:629–635, 2002.

[15] M. Haragus and G. Iooss. *Local Bifurcations, Center Manifolds, and Normal Forms in Infinite-Dimensional Dynamical Systems*. Springer, 2011.

[16] M.H. Holmes. *Introduction to perturbation Methods*. Springer-Verlag, 1995.

[17] Alexandra Jilkine and Leah Edelstein-Keshet. A comparison of mathematical models for polarization of single eukaryotic cells in response to guided cues. *PLoS Comput Biol*, 7:e1001121, 2011.

[18] J.K. Kevorkian and J.D. Cole. *Multiple Scale and Singular Perturbation Methods*. Springer-Verlag New York, 1 edition, 1996.

[19] E. Knobloch. Spatial localization in dissipative systems. *Annual Review of Condensed Matter Physics*, 6:325–359, 2015.

[20] G. Kozyreff and S.J. Chapman. Asymptotics of large bound state of localised structures. *Physical Review Letters*, 97:art.no.044502, 2006.

[21] David J.B. Lloyd and Hayley OFarrell. On localised hotspots of an urban crime model. *Physica D: Nonlinear Phenomena*, 253:23 – 39, 2013.

[22] R. Lockley, G. Ladds, and T. Bretschneider. Image based validation of dynamical models for cell reorientation. *Cytometry Part A*, 87(6):471–480, 2015.

[23] A.F.M. Marée, V.A. Grieneisen, and L. Edelstein-Keshet. How cells integrate complex stimuli: The effect of feedback from phosphoinositides and cell shape on cell polarization and motility. *PLoS Comput Biol*, page e1002402, 2012.

[24] H. Meinhardt. Orientation of chemotactic cells and growth cones: models and mechanisms. *Journal of Cell Science*, 12:867–74, 1999.
[25] M. Meron. *Nonlinear Physics of Ecosystems*. CRC Press, 3rd edition, 2015.
[26] Y. Mori, A. Jilkine, and L. Edelstein-Keshet. Wave-pinning and cell polarity from a bistable reaction-diffusion system. *Biophysical Journal*, 94:3684 – 3697, 2008.
[27] Y. Mori, A. Jilkine, and L. Edelstein-Keshet. Asymptotic and bifurcation analysis of wave-pinning in a reaction-diffusion model for cell polarization. *SIAM Journal on Applied Mathematics*, 71(4):1401–1427, 2011.
[28] J.D. Murray. *Mathematical Biology II: Spatial Models and Biomedical Applications*. Springer-Verlag, New York, 3rd edition, 2002.
[29] M. Otsuji, S. Ishihara, C. Co, K. Kaibuchi, A. Mochizuki, and S. Kuroda. A mass conserved reaction-diffusion system captures properties of cell polarity. *PLoS Computational Biology*, 3(6), 2007.
[30] P. Parra-Rivas, E. Knobloch, D. Gomila, and L. Gelens. Dark solitons in the lugiato-lefever equation with normal dispersion. *Phys. Rev. A*, 93:063839, Jun 2016.
[31] R.J.H. Payne and C.S. Grierson. A theoretical model for ROP localisation by auxin in Arabidopsis root hair cells. *PLoS ONE*, 4(12):e8337. doi:10.1371/journal.pone.0008337, 2009.
[32] Trong. P.K., E.M. Nicola, N.W. Goehring, K.V. Kumar, and S.W. Grill. Parameter-space topology of models for cell polarity. *New Journal of Physics*, 16, 2014.
[33] Y. Pomeau. Front motion, metastability and subcritical bifurcations in hydrodynamics. *Physica D: Nonlinear Phenomena*, 23:3 – 11, 1986.
[34] B. Rubinstein, B.D. Slaughter, and R. Li. Weakly nonlinear analysis of symmetry breaking in cell polarity models. *Physical Biology*, 9(4):045006, 2012.
[35] D. Sept and A.E. Carlsson. Modeling large-scale dynamic processes in the cell: polarization, waves, and division. *Quarterly Reviews of Biophysics*, 47:221–248, 2014.
[36] B.D. Slaughter, S.E. Smith, and R. Li. Symmetry breaking in the life cycle of the budding yeast. *Cold Spring Harbor Perspectives in Biology*, a003384, 2009.
[37] V Breña–Medina and Alan Champneys. Subcritical Turing bifurcation and the morphogenesis of localized patterns. *Phys. Rev. E*, 90:032923, 2014.
[38] G.R. Walther, A.F. Mareé, L. Edelstein-Keshet, and V.A. Grieneisen. Deterministic versus stochastic cell polarisation through wave-pinning. *Bull. Math. Biol.*, 74:2570–2599, 2012.
[39] P.D. Woods and A.R. Champneys. Heteroclinic tangles and homoclinic snaking in the unfolding of a degenerate reversible hamiltonianhopf bifurcation. *Physica D: Nonlinear Phenomena*, 129:147–170, 1999.
[40] Yuval R. Zelnik, Ehud Meron, and Golan Bel. Localized states qualitatively change the response of ecosystems to varying conditions and local disturbances. *Ecological Complexity*, 25:26 – 34, 2016.

Appendix A. Normal form calculation. The goal of this appendix is to determine analytically the co-dimension-two point in the parameter space where the amplitude of the patterns bifurcates from being *sub-critical* to *super-critical* in the vicinity of the spatial instability in the model (28). In order to find this point, we will compute the amplitude equation for the patterns up to third order by means of a normal form procedure (see [15] for more details). The co-dimension-two point corresponds to the point, in the spatial instability, where the third order coefficient in the amplitude equation vanishes (see [37]). Our starting point is the model

$$\partial_t u = \delta \partial_{xx} u + [F(u,v) - \varepsilon\theta u], \tag{28a}$$

$$\partial_t v = \partial_{xx} v - [F(u,v) - \varepsilon\alpha] \qquad x \in [-L, L]\,, \quad \partial_x(u,v)(\pm L) = 0, \tag{28b}$$

$$\text{where} \quad F(u,v) = \left(\gamma \frac{u^2}{1+u^2} + 1\right) v - \eta u = \psi(u) v - \eta u. \tag{28c}$$

For sake the of completeness, let us recall the expressions obtained in subsection 4.1. The homogeneous equilibrium and the critical curve where the spatial instability takes place are

$$u_0 = \frac{\alpha}{\theta}, \quad v_0 = \beta_0 + \varepsilon\beta_1 = \frac{\eta u_0}{\psi(u_0)} + \varepsilon \frac{\alpha}{\psi(u_0)}, \tag{29a}$$

$$0 = \varepsilon\theta\psi(u_0) - \frac{(\psi'(u_0)v_0 - (\psi(u_0)\delta + \eta + \varepsilon\theta))^2}{4\delta}, \tag{29b}$$

when:

$$k_c^2 = \frac{\psi'(u_0)v_0 - (\psi(u_0)\delta + \eta + \varepsilon\theta)}{2\delta} > 0.$$

The expression (29b) corresponds to (11) written in terms of ψ instead of the partial derivatives $\partial_u F, \partial_v F$. Evaluating the system (28) at the critical point (i.e. the parameters satisfying (29b)) and translating the system through the change of variables

$$(u, v) = (u_0, v_0) + (U, V),$$

we obtain the main equation of this appendix

$$\partial_t \begin{pmatrix} U \\ V \end{pmatrix} = [\mathbb{J} + \mathbb{D}\partial_{xx}]_c \begin{pmatrix} U \\ V \end{pmatrix} + \begin{pmatrix} 1 \\ -1 \end{pmatrix} \mathbb{NL}(U, V), \tag{30}$$

where

$$[\mathbb{J} + \mathbb{D}\partial_{xx}]_c = \begin{bmatrix} \delta\partial_{xx} + \psi'(u_0)v_0 - (\eta + \varepsilon\theta) & \psi(u_0) \\ \eta - \psi'(u_0)v_0 & \partial_{xx} - \psi(u_0) \end{bmatrix}_c, \tag{31}$$

$$\mathbb{NL}(U, V) = \psi'(u_0)UV + (v_0 + V)\sum_{n=2}^{\infty} \frac{\psi^{(n)}(u_0)}{n!} U^n. \tag{32}$$

Here, the sub-index c in the linear operator stands for the critical values of the parameters when one of them is fixed through (29b). In the remainder we will drop this sub-index assuming

that we are at the critical point. Using (31) and (32), we will compute the amplitude equation by using the normal form procedure. More precisely, we will look for the amplitude equation (33b), and the change of variables (33a) (which transforms from the original variables (u, v) into the new variable A) at the same time. This is respectively

$$\begin{pmatrix} U \\ V \end{pmatrix} = W^{[1]} + W^{[2]} + \dots, \tag{33a}$$

$$\partial_t A = \partial_t A^{[1]} + \partial_t A^{[2]} + \dots, \tag{33b}$$

where the superscript accounts for the order in A (in the remainder we will refer to this as "the order"). Formally, this equation must be solved at each order until it saturates (until the first coefficient obtained is negative in the region of parameters of interest). At that point, the amplitude equation is obtained *at the critical point*. An extra step, the *unfolding*, is necessary in order to allow the critical parameter to present a small variation around its critical value. Since we are only interested in the change of sign in the third coefficient, we will limit our calculations to that order. We are now in conditions to start the *normal form* procedure

Order 1

At order 1, (30) is

$$\partial_A W^{[1]} \partial_t A^{[1]} + c.c. = [\mathbb{J} + \mathbb{D}\partial_{xx}] W^{[1]},$$

here *c.c.* stands for *complex conjugate*. This abbreviation will be used in the rest of the appendix. Since we are interested in constructing a correction to the pattern solution, the first order corresponds to the linear approximation. This is equivalent to consider $\partial_t A^{[1]} = 0$. Replacing the following ansatz

$$W^{[1]} = \begin{pmatrix} w_1 \\ w_2 \end{pmatrix} (A e^{ik_c x} + \bar{A} e^{-ik_c x}),$$

and keeping in mind that the linear operator at the critical point is *singular*, the solution for $W^{[1]}$ is

$$W^{[1]} = \begin{pmatrix} \psi(u_0) \\ \delta k_c^2 - \psi'(u_0) v_0 + \eta + \varepsilon\theta \end{pmatrix} (A e^{ik_c x} + c.c.). \tag{34}$$

This expression is the same as (13).

End of Order 1.

Order 2

At order 2, (30) is

(35a)

$$\partial_A W^{[1]} \partial_t A^{[2]} + c.c. = [\mathbb{J} + \mathbb{D}\partial_{xx}] W^{[2]} + \begin{pmatrix} 1 \\ -1 \end{pmatrix} ((|A|^2 + c.c.) b_{20} + (A^2 e^{2ik_c x} + c.c) b_{22}),$$

$$b_{20} = \frac{1}{2} w_1 \left(v_0 \psi''(u_0) w_1 + 2\psi'(u_0) w_2 \right) = b_{22}. \tag{35b}$$

Since in the nonlinear terms there are not *secular terms* (terms which are proportional to the kernel of the linear operator (34)), we can take $\partial_t A^{[2]} = 0$. Actually, this is the case for every *even order* (i.e. $\partial_t A^{[2n]} = 0$). Taking into account this assumption, we can solve the equation at this order by proposing the following ansatz

$$W^{[2]} = \varphi_{20}(|A|^2 + c.c.) + \varphi_{22}(A^2 e^{2ik_c x} + c.c.). \tag{36}$$

In the remainder, we will carry out an analogous procedure for the different orders. Hence, it is useful to introduce the following notation to make the steps more clear. At the different orders, the scalar quantity multiplying different powers of A will be denoted by $b_{i,j}$ (see for example b_{20} in (35b)), where the first sub-index stands for the order and the second for the multiple of k_c in the exponent. The same labels are used in our ansatz (36) for the vectors $\varphi_{i,j}$. At this order, the uncoupled linear systems obtained are

$$\mathbb{J}\varphi_{20} = b_{20}\begin{pmatrix} -1 \\ 1 \end{pmatrix},$$

$$[\mathbb{J} - 4k_c^2\mathbb{D}]\varphi_{22} = b_{22}\begin{pmatrix} -1 \\ 1 \end{pmatrix}.$$

Solving these equations, we obtain the first correction in the change of variables (33a).

End of Order 2.

Order 3

Using the same notation introduced in the previous order, at order 3 the equation (30) is

$$[\mathbb{J} + \mathbb{D}\partial_{xx}]W^{[3]} = \begin{pmatrix} -1 \\ 1 \end{pmatrix}[b_{31}(|A|^2 Ae^{ik_c x} + c.c.) + b_{33}(A^3 e^{3ik_c x} + c.c.)]$$
$$+ (\partial_A W^{[1]}\partial_t A^{[3]} + c.c), \tag{37}$$

with the coefficients

$$b_{31} = \frac{1}{6}\Big\{3v_0\psi^{(3)}(u_0)w_1^3 + 12v_0\psi''(u_0)w_1\varphi_{20}^1 + 6v_0\psi''(u_0)w_1\varphi_{22}^1 + 9\psi''(u_0)w_2w_1^2$$
$$+12\psi'(u_0)w_1\varphi_{20}^2 + 12\psi'(u_0)w_2\varphi_{20}^1 + 6\psi'(u_0)w_1\varphi_{22}^2 + 6\psi'(u_0)w_2\varphi_{22}^1\Big\},$$
$$b_{33} = \frac{1}{6}\left(v_0\psi^{(3)}(u_0)w_1^3 + 6v_0\psi''(u_0)w_1\varphi_{22}^1 + 3\psi''(u_0)w_2w_1^2\right) + \psi'(u_0)w_1\varphi_{22}^2 + \psi'(u_0)w_2\varphi_{22}^1.$$

In contrast with the previous case, here we can notice the existence of secular terms (this is the case for every *odd order*). In order to ensure the solvability of this equation we make use of the *solvability condition* (or *Fredholm Alternative* theorem)[15]. Considering the following inner product

$$\langle \vec{v}_0 f(x) | \vec{w}_0 g(x)\rangle = \frac{1}{X}\int_y^{y+X} f^*(x)g(x)dx\vec{v}_0 \cdot \vec{w}_0, \tag{38}$$

the adjoint of the linear operator is:

$$[\mathbb{J} + \mathbb{D}\partial_{xx}]^\dagger = [\mathbb{J}^t + \mathbb{D}\partial_{xx}],$$

and therefore the kernel of this operator is:

$$W^\dagger = \begin{pmatrix} w_1^\dagger \\ w_2^\dagger \end{pmatrix} (e^{ik_c x} + e^{-ik_c x}) = \begin{pmatrix} \psi'(u_0)v_0 - \eta \\ -\delta k_c^2 + \psi'(u_0)v_0 - \eta - \varepsilon\theta \end{pmatrix} (e^{ik_c x} + e^{-ik_c x}).$$

Hence, according to the solvability condition, it is enough to ensure the orthonormality between the right hand side of (37) and the kernel of the adjoint operator to ensure the solvability of problem (37).

Moreover, under the scalar product given by (38), the following *orthonormality* relation is satisfied

$$\frac{1}{X}\int_y^{y+X} e^{-imk_c x} e^{ink_c x} dx = \delta_{n,m}.$$

Then, the *solvability condition* is reduced in this case to the following expression

$$\partial_t A^{[3]} \langle \begin{pmatrix} w_1 \\ w_2 \end{pmatrix} | \begin{pmatrix} w_1^\dagger \\ w_2^\dagger \end{pmatrix} \rangle + \langle \begin{pmatrix} -1 \\ 1 \end{pmatrix} | \begin{pmatrix} w_1^\dagger \\ w_2^\dagger \end{pmatrix} b_{31} \rangle |A|^2 A = 0,$$

solving for $\partial_t A^{[3]}$

$$\partial_t A^{[3]} = \frac{\langle \begin{pmatrix} 1 \\ -1 \end{pmatrix} | \begin{pmatrix} w_1^\dagger \\ w_2^\dagger \end{pmatrix} \rangle}{\langle \begin{pmatrix} w_1 \\ w_2 \end{pmatrix} | \begin{pmatrix} w_1^\dagger \\ w_2^\dagger \end{pmatrix} \rangle} b_{31} |A|^2 A = C_3 |A|^2 A.$$

By imposing this condition in (37), we can solve the equation at this order by introducing the ansatz

$$W^{[3]} = \varphi_{31}(|A|^2 A e^{ik_c x} + c.c.) + \varphi_{33}(A^3 e^{3ik_c x} + c.c.)$$

The uncoupled *solvable* linear systems are

$$[\mathbb{J} - k_c^2 \mathbb{D}]\varphi_{31} = \begin{pmatrix} w_1 \\ w_2 \end{pmatrix} C_3 + \begin{pmatrix} -1 \\ 1 \end{pmatrix} b_{31}$$

$$[\mathbb{J} - 9k_c^2 \mathbb{D}]\varphi_{33} = \begin{pmatrix} -1 \\ 1 \end{pmatrix} b_{33}$$

By solving these systems we obtain the change of variables at this order

End of Order 3.

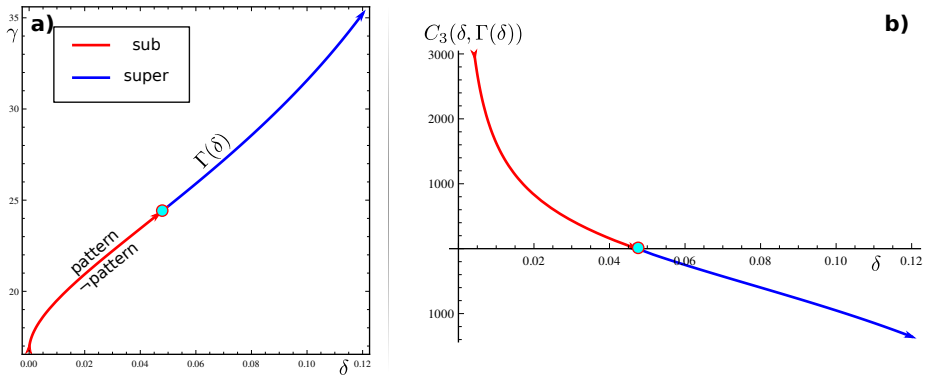

Figure 15. *Determination of the co-dimension-two point for the parameter values* $\varepsilon = 1, \gamma \in [11, 35], \delta \in [0, 0.12], \eta = 5.2, \theta = 5.5, \alpha = 1.5$ ***a)*** *The critical curve has been parameterised as* $\Gamma(\delta)$*. In* ***b)****, a plot of* C_3 *as a function of the critical curve is presented. The existence of a zero (light blue dot) changes the nature of the amplitude equation from sub-critical (red) and super-critical (blue).*

Now that an analytic expression for cubic coefficient C_3 has been determined, we can look for a change of sign along the critical curve.

All the corrections and coefficients obtained throughout this procedure depend on the previous orders. Even though obtaining closed-form expressions is possible, it is in general cumbersome. Hence, the use of a symbolic algebra software is strongly recommended. In order to illustrate our calculations, Figure 15 shows the existence of a co-dimension-two point in the parameter space. Allowing δ and γ to vary and fixing the rest of the parameters as in subsection 4.1, we parameterise the critical curve (29b) (blue and red line in Figure 15 (a)) as a function $\Gamma(\delta)$). Hence, $C_3(\Gamma(\delta), \delta)$ is a single variable function which presents one zero (light blue dot in Figure 15), changing the nascence of spatial patterns from being *super-critical* (blue) to *sub-critical* (red). The existence of a region where a sub-critical amplitude take place guarantee the existence of a bi-stability region between homogeneous equilibrium and spatial patterns. Within that region, a sub-region where localised structures exist could be found. Therefore, a point in the parameter space below the critical curve and in the sub-critical region is an educated guess of a starting point in the search for localised structures. As a final remark, when the sub-critical bifurcation for the amplitude takes place, as we pointed out above, a higher order correction must stabilise the spatial patterns. From the numerics on the full model, we know that the patterns are stable and therefore, this further correction have not been computed.